Johannes Niederwieser

Modelling, Monitoring and Control of a Renewable Redox Flow Battery

Master's Thesis

to achieve the university degree of
Diplom-Ingenieur

submitted to
Graz University of Technology

Supervisor
Univ.-Prof. Dipl.-Ing. Dr.techn. Martin Horn

Cosupervisor
Dipl.-Ing. Dr.techn. Markus Gölles

Institute of Automation and Control

Graz, October 2024

Affidavit

I declare that I have authored this thesis independently, that I have not used other than the declared sources/resources, and that I have explicitly indicated all material which has been quoted either literally or by content from the sources used. The text document uploaded to TUGRAZonline is identical to the present master's thesis.

Date

Signature

Abstract

Regarding the rapid rise in renewable but volatile energy sources, energy storages like redox flow batteries are considered key for future electricity supply. Based on a test bench this work investigates a new type of redox flow battery with an electrolyte, which can be synthesised from lignin one of the main substances of biomass and typical waste product of the paper industry. This work hereby focuses onto two aspects of the operation of these batteries:
The first one is the development of a model to describe the hydraulics of the battery. Based on this model a control structure is proposed, which on the one hand allows the tracking of a reference volume flow, while on the other hand prevents high pressure differences across the membrane.
The second aspect focuses on the determination of the so called State-of-Charge, which is a key variable of interest for the operation on the grid. Therefore an electrochemical model is developed to describe the processes inside the redox flow battery, which then is parametrized by particle swarm optimization using measurement data of the redox flow battery test bench. Based on this electrochemical model an observer from literature is adopted to estimate the State-of-Charge and additionally the maximum storable charge of both electrolytes of the redox flow battery from two redox potential measurements inside the tanks.

Contents

1. Introduction and motivation

The electric power grid is undergoing a rapid change. Increased use of renewable energy sources like wind and photovoltaic, which are only available at certain times, make balancing production and demand increasingly difficult. To ensure grid operation under this circumstances, grid-scale energy storage is widely believed to be necessary [1].

One of the most promising options for large scale energy storage are redox flow batteries, RFBs, [2, 3], since RFBs are not dependent on geologic suitable structures, like mountainous terrain for pumped hydro electric storages and mines or natural cavities for compressed air energy storage [4]. Compared to other battery technologies, RFBs have a longer lifetime of up to multiple decades while having a good efficiency [5]. The basic structure of RFBs consists out of two tanks filled with electrolytes containing two different redox couples in it. Redox couples are two species which react via an electro-chemical rection in one another. These electrolytes are pumped through the battery cells, consisting of two electrodes each in contact with one of the electrolytes separated by a membrane. The electro-chemical reactions, happening at the electrodes, either release or store energy.

Among the different types of RFBs developed so far, the all-vanadium RFB is currently the most mature system, with several grid scale batteries already in operation all over the world. Since only a few countries worldwide control the world's vanadium supply, it is classified as critical raw material by the European Union's critical raw material act. Therefore, extensive research in alternatives to vanadium for redox flow batteries is done. Promising research on vanillin-based electrolytes for organic RFBs [6], suggests a local available and cheap electrolyte as alternative to vanadium. Till now, these vanillin-based electrolytes were only tested in small laboratory-scale single cell RFBs. Though these laboratory-scale RFBs are useful to test basic electrolyte properties, their different structure cannot replicate all the phenomena occurring in operation of a grid-scale RFB. To investigate these vanillin-based electrolytes in a grid-scale-like RFB, a RFB test bench was installed, with a structure representative for grid-scale RFBs.

Essential for the operation of a RFB is the supply of enough reactants to the battery cells, which is provided by an sufficient volume flow of the electrolytes. Grid-scale RFBs most often use centrifugal pumps, as so does the RFB test bench, while these laboratory-scale RFBs use peristaltic pumps. The main advantage of these peristaltic pumps here is, that they pump a fixed amount of fluid per rotation, which makes them easy to control the volume flow and a suitable choice for laboratory-scale RFBs. For grid-scale RFBs peristaltic pumps are not used because of their disadvantages, low efficiency and pulsed flow. Centrifugal pumps are a more suitable choice, but the control of the volume flow is more

sophisticated. Additionally to the control of the volume flow the pressure difference across the membrane should be hold close to zero. This on the one hand reduces stress and prevents rupture of the membrane and on the other hand also reduces inverse osmosis across the membrane. The first goal of this thesis is to develop an effective control structure, which fulfils these objectives. Therefore, chapter 3 focuses on the hydraulics of RFBs, beginning with the modelling of the hydraulics in section 3.1, based on the structure of the RFB test bench, described in chapter 2. Based on this model a suitable control structure will be developed and also tested on the RFB test bench in section 3.2.

To allow the operation of RFBs for grid balancing tasks one key variable has to be known, the State-of-Charge (SOC). It is a measure on how much energy currently is stored in the RFB. Only the knowledge of the SOC enables the incorporation of RFBs into energy management systems. Unfortunately the SOC can not be measured directly. Therefore, chapter 4 focuses on the electro-chemistry of the vanillin-based RFBs, beginning with the modelling of the electro-chemistry in section 4.1. Based on conducted experiments on the RFB test bench this model then is parametrized in section 4.2. Finally, a state observer based on the parametrized model is applied onto measurement data to estimate the SOC online in section 4.3.

Finally chapter 5 concludes the thesis and gives an outlook on future work to be done in the field of renewable redox flow batteries.

2. Description of the redox flow battery test bench

Since all the modelling and validation in this thesis is based on experiments, see Appendix A, conducted on the RFB test bench, the knowledge of its structure will be necessary to understand all the following chapters. Therefore, this chapter explains the working principle of an RFB paired with the explanation of the structure of the RFB test bench.
The most fundamental part of every battery is the battery cell. The structure of one battery cell of the RFB test bench can be seen in Figure 2.1. One battery cell consists out of two electrodes, whose surface area is extended by two carbon felts [7]. The two sides are separated by a semi-permeable membrane, which only allows hydrogen ions to pass through. The reactants or redox-active substances are dissolved within two different elec-

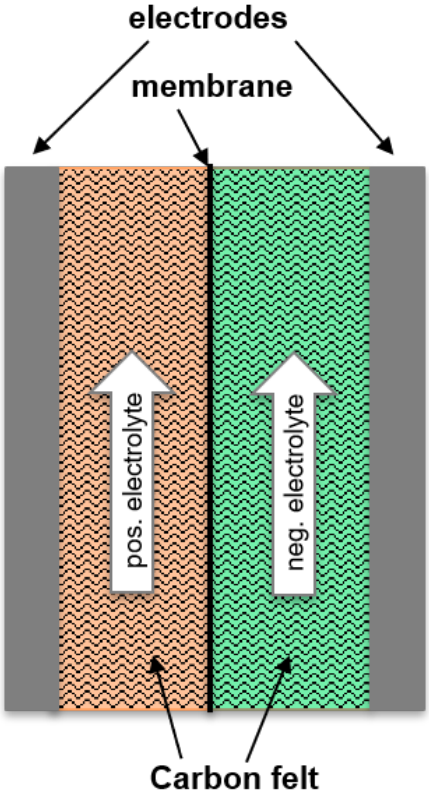

Figure 2.1.: Structure of one battery cell.

trolytes, which fill the empty spaces in the carbon felts. To increase the storable energy the electrolytes are pumped through the cell and are stored in tanks outside. The electrolyte

with the higher potential, will be called positive electrolyte and the electrolyte with the lower potential, will be called negative electrolyte. The electrolytes of the RFB test bench use 0.5 $\frac{mol}{l}$ phosphoric acid, H_3PO_4, in aqueous solution as the supporting electrolyte, where the redox-active substances are dissolved. The negative electrolyte uses the two substances anthraquinone-2,6-disulfonate AQDS and anthrahydroquinone-2,6-disulfonate AHQDS as its redox active substances. The positive electrolyte redox active substances are methoxyquinonesalt MQS and methoxyhydroquinonesalt MHQS. For readability, only the abbreviations will be used.
While charging MHQS reacts to MQS at the surface of the carbon felt. Thereby electrons and hydrogen ions are released. The electrons are absorbed by the electrode, whereas the hydrogen ions diffuse through the membrane. On the other side of the membrane hydrogen ions, electrons and AQDS react and form AHQDS. The same process happens in reverse for discharge of the battery.
To increase the usable voltage many battery cells are typically connected in series electrically to one battery stack. The electrolytes are pumped hereby in a hydraulic parallel manner through this battery stack. For the RFB test bench investigated the stack consists of 8 cells. Figure 2.2 shows the structure of this stack, with the hydraulic parallel structure.

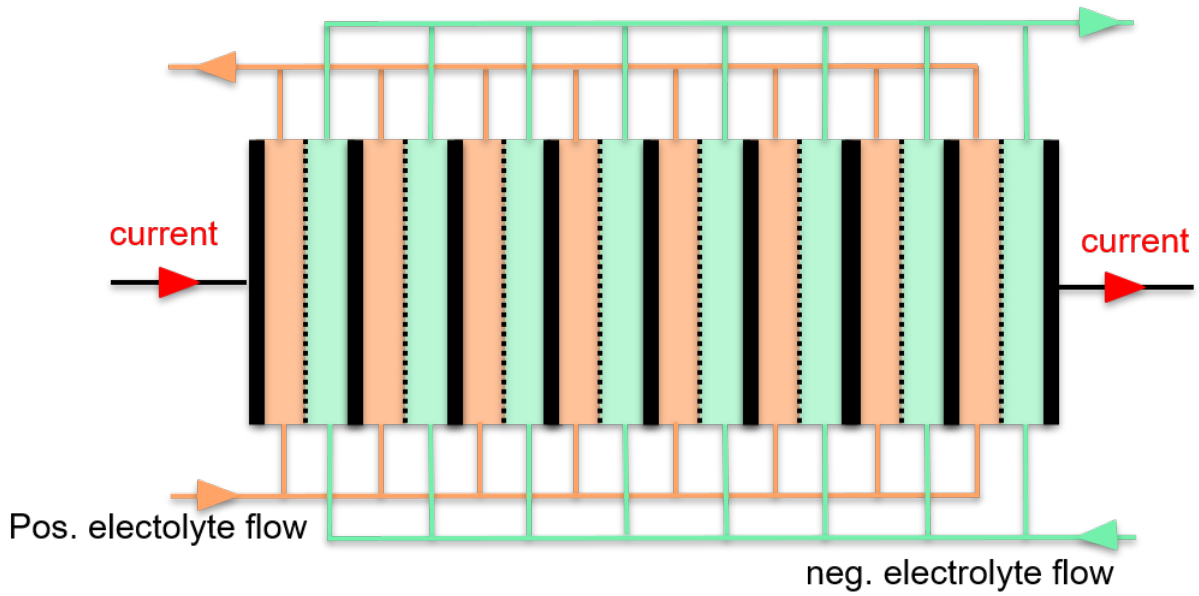

Figure 2.2.: Structure of the stack of the RFB test bench.

The structure of the RFB test bench can be seen in Figure 2.3. It consists of two seperate hydraulic circuits for both of the electrolytes and the electric circuit. Each hydraulic circuit consists of a tank containing the electrolyte and a centrifugal pump, with pipes delivering the electrolyte to the stack and back to the tank. In the return pipe a needle valve allows the adjustment of the flow resistance. To enable the emptying of the stack into the tank, when the pump is switched off, the stack is elevated above the tank and the end of the return pipe in the tank is situated above the fluid surface. To enable the monitoring the pressure difference across the membrane, at each inlet and outlet of the stack a pressure

sensor allows to measure pressure relative to the ambient air pressure. The flow of the positive electrolyte is measured with an ultrasonic sensor in the return pipe. The measurement of one volume flow is sufficient, since the volume flows of both hydraulic circuits should be close to one another. This is because the hydraulic circuits of both electrolytes have the same number of bends and similar length of the pipes. But if necessary for some experiments, the flow sensor can be moved to the negative electrolyte side. The redox potentials, also called half-cell potentials, are measured with two silver/silver chloride or Ag/AgCl redox probes in the feed pipes of the pumps. Since the redox probes tend to drift slowly over time, recalibration of the redox probes is necessary before each experimental campaign.

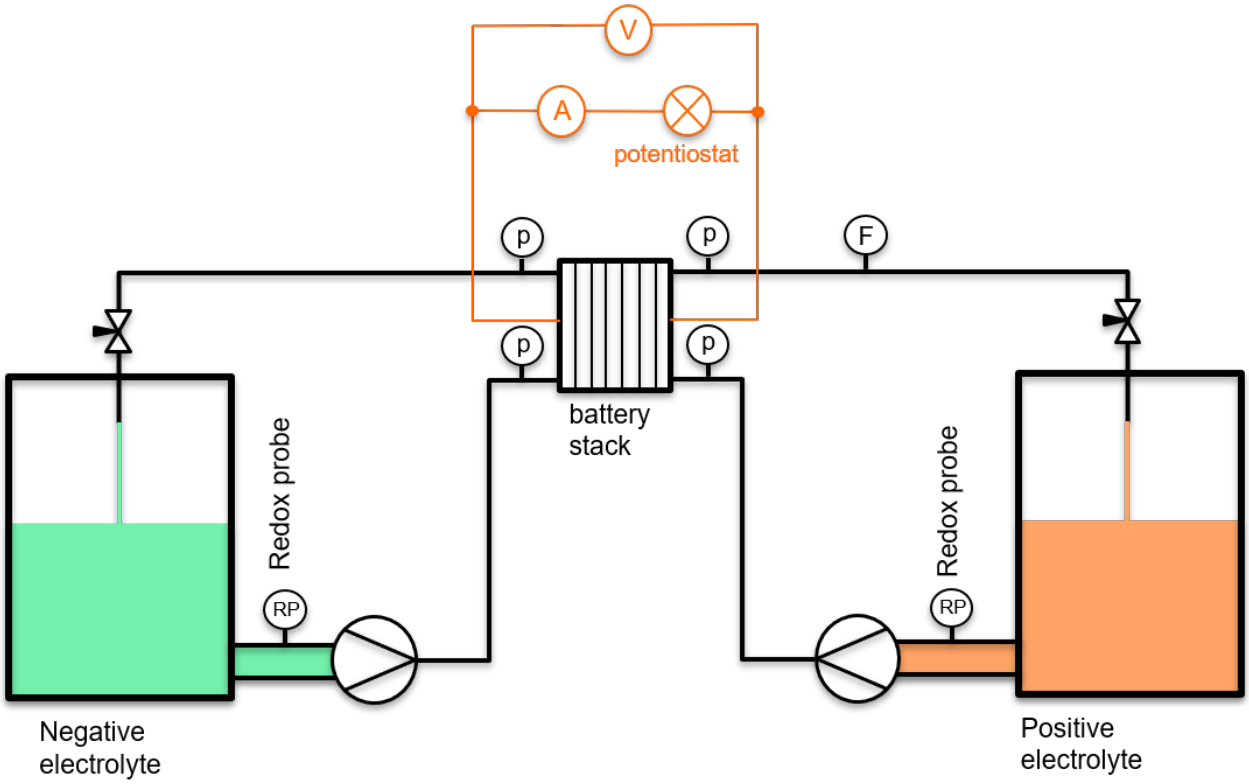

Figure 2.3.: Schematic structure of the renewable redox flow battery test bench.

The electric circuit consists of the stack, a measurement of the stack voltage, a measurement of the current and a potentiostat, which emulates different modes of operation. The potentiostat acts as a source while charging and as a load while discharging. Thereby the potentiostat either provides constant voltage or constant current dependent on the conducted experiment. The potentiostat also limits the applied voltage according to predefined boundaries to avoid electrolysis in the battery stack.

3. Hydraulics

The hydraulics play a crucial role for redox flow batteries. Only a sufficient volume flow can ensure that there are enough reactants in the battery stack. In this chapter, a model describing the hydraulics is developed (section 3.1), and based on this model, a control structure tracking a given reference is developed and tested (section 3.2).

3.1. Modelling of the hydraulics

All pressure measurements of the test bench are pressure measurements relative to ambient pressure. All pressures relative to ambient are expressed by p in all the following formulas. Pressure differences over components of the system are expressed with Δp.
The hydraulics consist of basically two hydraulic circuits with the same structure. There might be coupling between these two hydraulic circuits due to mechanical deformation of the membrane as a result of a pressure difference over the membrane. But since the pressure difference should be hold close to zero to avoid damage this coupling can be neglected. Also, one aim of the controller design will be to drive the pressure difference towards zero. So the coupling effects will have little to no effect on the systems' behaviour for experiments in the future. Because of this coupling is neglected and the similarity of the two hydraulic circuits, it is enough for the derivation of the model to investigate only one of these hydraulic circuits, but the parametrization of the model will be done for both hydraulic circuits separately.
The schematic structure of one hydraulic circuit can be seen in Figure 3.1. It consists of the tank, connected to the pump via a wide tube, a feed pipe from the pump to the battery stack, the stack itself and a return pipe from the stack back to the tank. Directly before and after the stack pressure measurements are made, and in the return pipe, the volume flow is measured. A needle valve at the end of the return pipe enables the manual adaptation of the return pipe's flow resistance if necessary. In operation, there exists a small constant overpressure p_{N_2} (< 0.05 bar) inside the tank caused by the infusion of pure nitrogen gas for an oxygen free environment. Manually measured heights, which will be used for modelling, are also defined in Figure 3.1. For the derivation of the model the hydraulic system it is assumed that the stack and the pipes are fully filled with the electrolyte, such that no bubbles are trapped inside the stack or the pipes.
The first part of the modelling is the description of the behaviour for quasi-stationary flow. Therefore the pump, the pipes and the stack will be investigated separately in section 3.1.1 and will be combined to one quasi stationary model in section 3.1.2. The last step is the description of the dynamic behaviour in section 3.1.3.

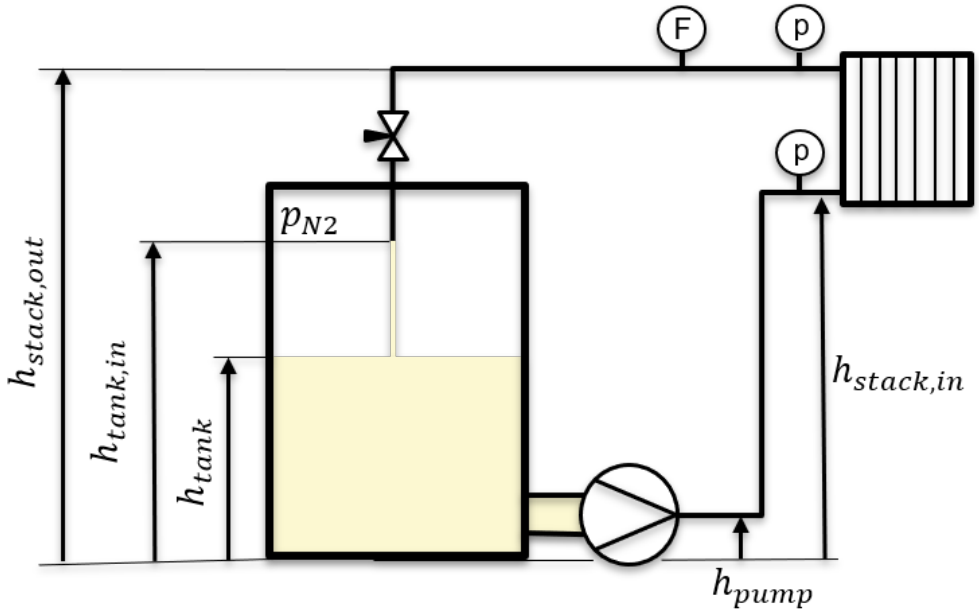

Figure 3.1.: Schematic structure of one side of the hydraulics.

3.1.1. Modelling of the different hydraulic parts for quasi-stationary flow

This section describes the modelling of the hydraulic behaviour of the pump in section 3.1.1.1, the pipes in section 3.1.1.2 and the stack in section 3.1.1.3.

3.1.1.1. Modelling of a centrifugal pump

The modelling of the centrifugal pump is based on the model described in [8]. Here the suggested model describing the quasi stationary behaviour of centrifugal pumps uses the pump's characteristic curve given by the datasheet. The characteristic curve shows the relation between volume flow $\dot{V}$ and pressure difference Δp_{pump} for the maximal rotational speed n_{max} of the pump. Sometimes multiple curves for different rotational speeds are available. The characteristic curve can be expressed as the quadratic function

$$\Delta p_{\text{pump,max}}(\dot{V}) = c_1 + c_2\dot{V} + c_3\dot{V}^2 \tag{3.1}$$

with the coefficients c_1, c_2 and c_3. By applying the affinity laws of centrifugal pumps

$$\frac{\dot{V}_2}{\dot{V}_1} = \frac{n_2}{n_1} \tag{3.2}$$

$$\frac{\Delta p_{\text{pump,2}}}{\Delta p_{\text{pump,1}}} = \left(\frac{n_2}{n_1}\right)^2 \tag{3.3}$$

the pressure can be described as a function of rotational speed and volume flow

$$\Delta p_{\text{pump}}(n, \dot{V}) = an^2 + bn\dot{V} + c\dot{V}^2, \tag{3.4}$$

where $a = \frac{c_1}{n_{\max}^2}$, $b = \frac{c_2}{n_{\max}}$ and $c = c_3$. For pumps with feedback speed control, where there is a linear relation between the control voltage and rotational speed of the pump in stationary operation, it is even possible to exchange n with the proportional control voltage u_n:

$$\Delta p_{\text{pump}}(u_n, \dot{V}) = \alpha u_n^2 + \beta u_n \dot{V} + \gamma \dot{V}^2, \tag{3.5}$$

Because there were two different and contradicting characteristic curves for the used pump available online, the pump had to be characterized by an experiment. The schematic setup for the experiment can be seen in Figure 3.2. The inlet of the pump is connected to

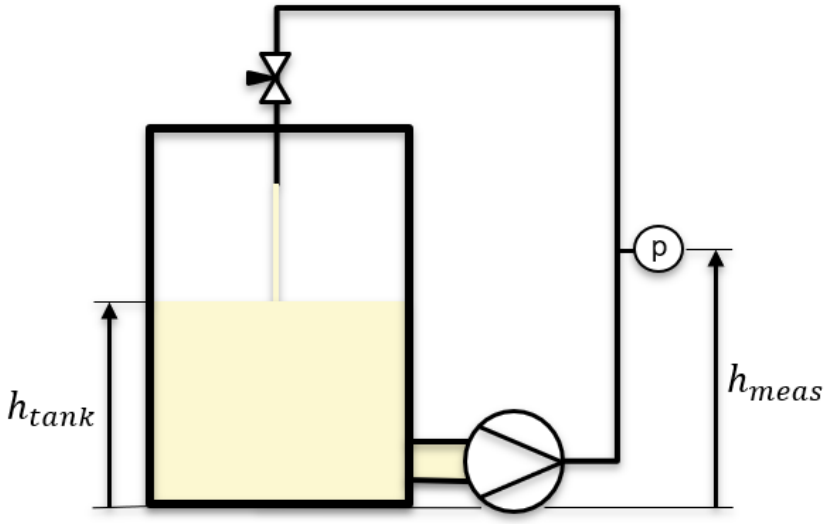

Figure 3.2.: Experimental setup to characterize the pump.

the tank and the pipe attached on the outlet of the pump feeds the electrolyte back to the tank. An additional needle valve makes it possible to adapt the flow resistance of the pipe. The pressure measurement is positioned after the pump at a height h_{meas}. At the time of the experiment in the tank there was ambient pressure.
For the measurements, the control voltage was fixed, while the flow resistance was changed by opening or closing of the needle valve. The characteristic curves were measured for the control voltages 4 V, 6 V, 8 V and 10 V. The measurements revealed an unknown and non-ideal property of the used pump, which is that for a control voltage of 8.9 V the pump reaches its maximum performance and stays there for higher control voltages. So the characteristic curve measured at a control voltage of 10 V is equivalent to the characteristic curve at 8.9 V. The measured data was corrected by subtracting the geodetic pressure difference $\Delta p_{\text{geo}} = \rho g(h_{\text{tank}} - h_{\text{meas}})$, with ρ as the density of the electrolyte and g as the gravitational acceleration.
Figure 3.3 shows the measured pump data and the model from equation (3.5) fitted by a least square approach to the uppermost curve corresponding to the maximal pump voltage of $8.9V$. It can be easily seen that the model works quite well in the upper region, but for the lower two curves the model and the measurements differ drastically. The

reason is probably that the used pump is speed controlled in a feedforward manner, which can't guarantee a linear behaviour between the control voltage and the rotational speed. It has to be noted, that this effect most certainly only exists for this small size centrifugal pump used and would not appear for bigger pumps controlled in an feedback manner with a frequency converter.
To improve the pump model for lower control voltages an additional correction function

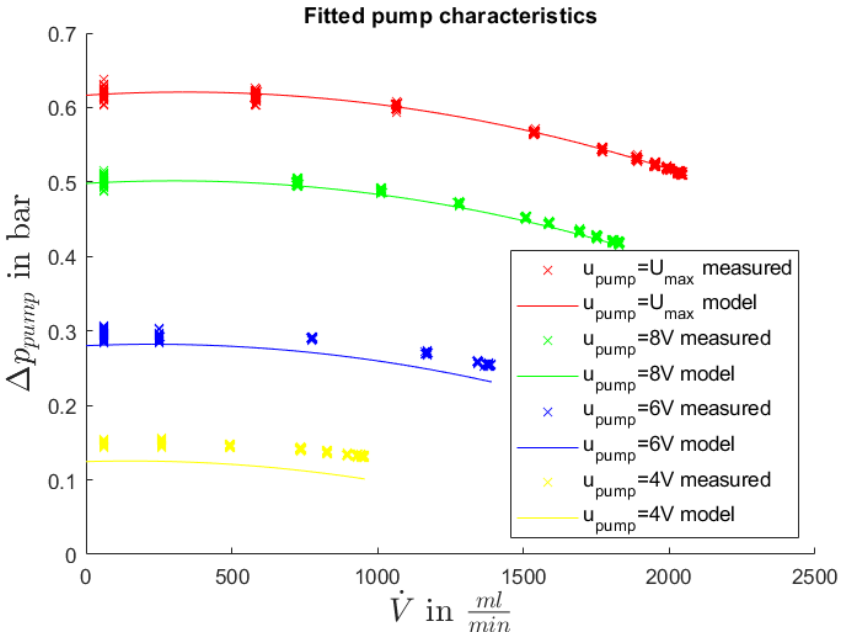

Figure 3.3.: Characteristic curves of the pump fitted without correction function.

$$u_n = u_{\text{pump}}^{0.9} \tag{3.6}$$

is introduced, which tries to compensate the nonlinear relation between control voltage u_{pump} and the velocity proportional quantity u_n. Figure 3.4 shows the pump model fitted with this additional correction function. It overall fits much better to the measured data. So the pump model including this correction function will be used for the description of the pump in this thesis.

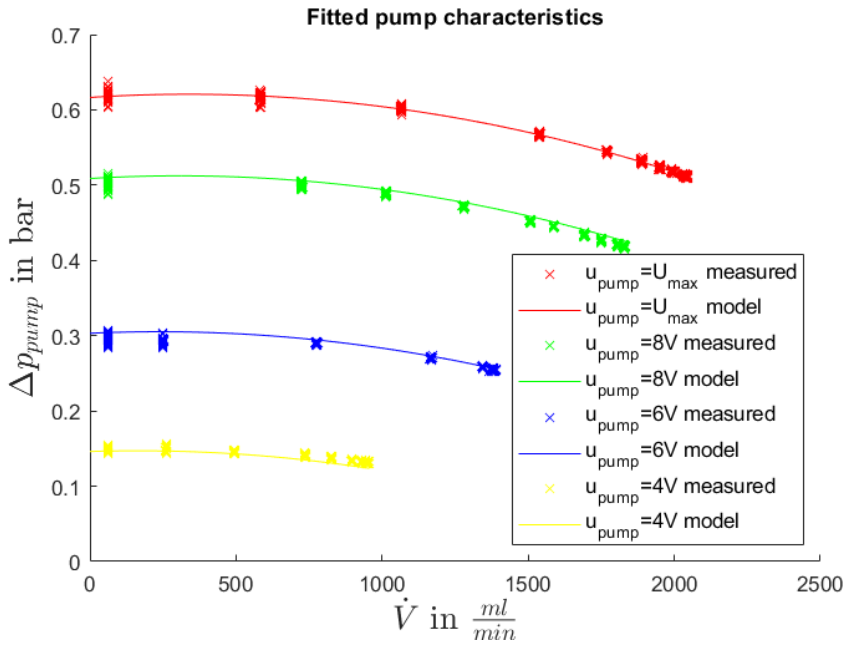

Figure 3.4.: Characteristic curves of the pump fitted with correction function.

3.1.1.2. Modelling of the flow resistances of the pipes

The pressure drop along the pipes is assumed to be dominated by the multiple bends of the pipes and the needle valves. Both bends and needle valves can be associated with pressure drops proportional to the volume flow squared. So for the pressure drop along the feed and return pipes the ansatz

$$\Delta p = R\dot{V}^2 \tag{3.7}$$

is used, where Δp is the pressure drop, R the flow resistance and $\dot{V}$ the volume flow. By applying Bernoulli's equation, the pressure at the measurement position at the output of the stack $p_{\text{stack,out}}$ can be expressed as

$$p_{\text{stack,out}} = p_{\text{N2}} - \rho g \Delta h_{\text{return}} + R_{\text{return}}\dot{V}^2 \tag{3.8}$$

, where p_{N2} is the pressure in the tank, $\Delta h_{\text{return}} = h_{\text{stack,out}} - h_{tank,in}$ is the height difference between tanks inlet and the position of the measurement, ρ is the density of the electrolyte, g is the gravitational acceleration and R_{return} is the hydraulic resistance of the return pipes bends and the needle valve. The pressure measurements at the input of the stack $p_{\text{stack,in}}$ can be expressed as

$$p_{\text{stack,in}} = p_{\text{N2}} + \rho g(h_{\text{tank}} - h_{\text{stack,in}}) + \Delta p_{\text{pump}}(u_{\text{pump}}, \dot{V}) - R_{\text{feed}}\dot{V}^2 \tag{3.9}$$

, where h_{tank} is the fill height of the tank, $h_{\text{stack,in}}$ is the height of the position of the measurement, Δp_{pump} is the pressure increase caused by the pump (see section 3.1.1.1) and R_{feed} is the hydraulic resistance of the feed pipes bends. To identify the unknown parameters R_{feed} and R_{return}, a least square approach is used. Figure 3.5 shows the model for the return pipe fitted to the measurement data. The assumption of the quadratic relation of flow and pressure drop coincides with the measurements.

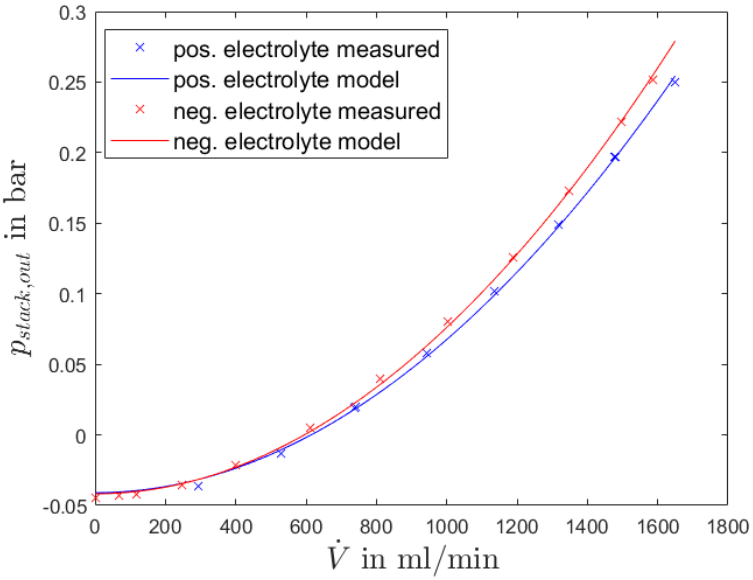

Figure 3.5.: Output pressure of the stack for both hydraulic circuits.

3.1.1.3. Modelling of the pressure flow relationship of the stack

The pressure difference over the stack Δp_{stack} is mainly caused by the effects of the carbon felt. The fibres of the carbon felt cause turbulences, but the assumption of pure turbulent flow turns out to be insufficient to describe the behaviour. To describe the pressure drop over the stack, a combination of a linear and a quadratic term is used as model:

$$\Delta p_{\text{stack}}(\dot{V}) = R_{\text{lin}}\dot{V} + R_{\text{quad}}\dot{V}^2 \tag{3.10}$$

The two parameters R_{lin} and R_{quad} are determined using the least squares method. In Figure 3.6 the pressure difference over the stack can be seen for both hydraulic circuits. The approach from equation (3.10) is able to capture the behaviour of the measured data quite well.

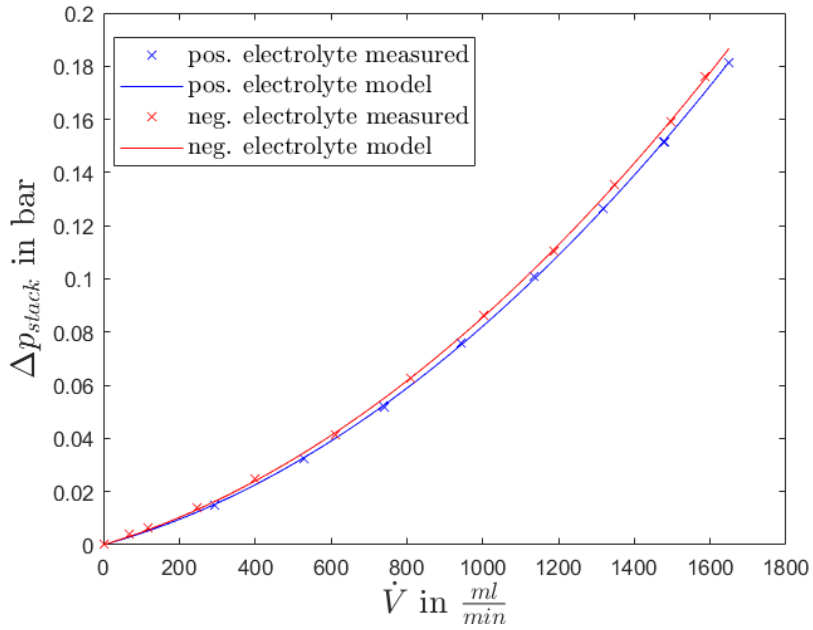

Figure 3.6.: Pressure difference to flow behaviour for the stack.

3.1.2. Hydraulic model for quasi stationary flow

The stationary model now combines all modelled parts from section 3.1.1. Figure 3.7 shows the schematic hydraulic circuit, where the arrows indicate pressure drops as analogy to voltage drops in electric circuits. At the inlet of the pump, a pressure of $p_{N_2} + \rho g(h_{\text{tank}} - h_{pump})$ is acting, consisting of the pressure in the tank due to nitrogen infusion p_{N_2} and the pressure due to the fill height of the tank h_{tank} in respect to the height of the pumps inlet h_{pump}. The pump causes an pressure increase $\Delta p_{\text{pump}}(u_{\text{pump}}, \dot{V}$ according to the model described in section 3.1.1.1. The pressure drop from the pump to the inlet of the stack (measurement position) is described by the pressure difference due to the height difference of stack inlet and pump $\Delta h_{\text{feed}} = h_{\text{stack,in}} - h_{\text{pump}}$ and the pressure loss due to the volume flow $\Delta p_{\text{feed}}(\dot{V})$, described in 3.1.1.2. The pressure drop at the stack also consists of a pressure difference due to the height difference of stacks inlet and outlet $\Delta h_{\text{stack}} = h_{\text{stack,out}} - h_{\text{stack,in}}$ and the pressure loss due to the volume flow $\Delta p_{\text{stack}}(\dot{V})$, described in section 3.1.1.3. The pressure drop from the stack outlet (measurement potition) consists of the pressure difference due to the height difference between outlet of the stack and inlet into the tank $\Delta h_{\text{return}} = h_{\text{stack,out}} - h_{\text{tank,in}}$ and the pressure drop due to the volume flow $\Delta p_{\text{return}}(\dot{V})$, described in section 3.1.1.2. At the inlet into the tank, only the pressure due to nitrogen infusion p_{N_2} is present.

The sum of all pressure differences along the hydraulic circuit has to be zero. This results in the equation:

$$\rho g(h_{\text{tank}} - h_{\text{tank,in}}) + \Delta p_{\text{pump}}(u_n, \dot{V}) - \Delta p_{\text{feed}}(\dot{V}) - \Delta p_{\text{stack}}(\dot{V}) - \Delta p_{\text{return}}(\dot{V}) = 0 \quad (3.11)$$

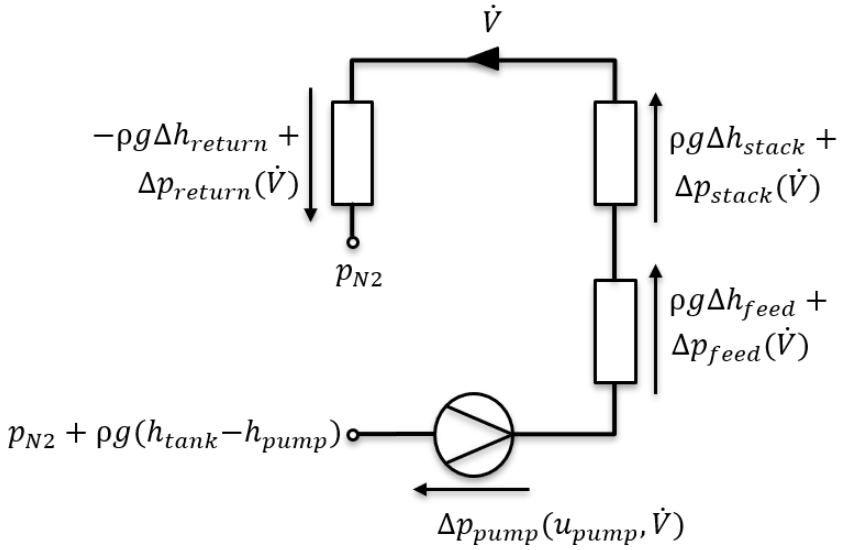

Figure 3.7.: Circuit diagram of the hydraulic model.

By inserting the models for the pump (section 3.1.1.1), the pipes (section 3.1.1.2) and the stack (section 3.1.1.3, one gets:

$$\rho g(h_{\text{tank}} - h_{\text{tank,in}}) + \alpha u_n^2 + \beta u_n \dot{V} - R_{\text{stack,lin}} \dot{V} + \underbrace{(\gamma - R_{\text{feed}} - R_{\text{stack,quad}} - R_{\text{return}})}_{R_{\text{ges,quad}}} \dot{V}^2 = 0 \tag{3.12}$$

This is a quadratic function in terms of the volume flow $\dot{V}$, which can be solved explicitly. Hereby, one of the solutions has no physical interpretation and can be neglected. So the volume flow in steady state $\dot{V}_{\text{s}}$ can be expressed as a function of u_n:

$$\dot{V}_{\text{s}}(u_n) = \frac{\beta u_n - R_{\text{stack,lin}}}{2R_{\text{ges,quad}}} + \sqrt{\left(\frac{\beta u_n - R_{\text{stack,lin}}}{2R_{\text{ges,quad}}}\right)^2 + \frac{\alpha u_n - \rho g(h_{\text{tank}} - h_{\text{tank,in}})}{R_{\text{ges,quad}}}} \tag{3.13}$$
$$\text{where } u_n = u_{\text{pump}}^{0.9}$$

So in combination with the correction function $u_n = u_{\text{pump}}^{0.9}$, the steady state flow $\dot{V}_{\text{s}}$ can also be expressed as a function of the pump control voltage u_{pump}.
Using all the previously identified parameters in equation (3.13) to calculate the steady state of the volume flow doesn't fit well to the measured data. The reason is not entirely clear. Further investigations would be needed to identify the reason for this mismatch.
To get a parameter set, which better fits to the data, an optimization based approach which considers all the measured data at once is used. Therefore, the equations (3.8), (3.9) and (3.12) are used. By the assumption that the pump parameters are correctly identified, so the optimization vector x_{par} contains only the parameters h_{tank}, $h_{\text{tank,in}}$, $h_{\text{stack,in}}$, $h_{\text{stack,out}}$ and the flow resistances for positive and negative electrolyte side. The heights are included into the optimization vector, because some of them are not easy to measure directly. Heights or height differences which were measured are included into a cost function $J_{\text{h}} = \sum_{i=1}^{N_h} (h_i - h_{i,meas})^2$. For equation (3.12) the left-hand side is used as a

model error measure $e_{1,i}$ for the i-th measurement data point.

$$e_{1,i} = \rho g(h_{\text{tank}} - h_{\text{tank,in}}) + \Delta p_{\text{pump}}(u_{\text{pump},i}, \dot{V}_i) - R_{\text{stack,lin}}\dot{V}_i - (R_{\text{feed}} + R_{\text{stack,quad}} + R_{\text{return}})\dot{V}_i^2 \tag{3.14}$$

The error measures $e_{2,i}$ and $e_{3,i}$ are the measured pressure minus the pressure predicted by the equations (3.8) and (3.9).

$$e_{2,i} = p_{\text{N2}} - \rho g \Delta h_{\text{return}} + R_{\text{return}}\dot{V}_i^2 - p_{\text{stack,out},i} \tag{3.15}$$

$$e_{3,i} = p_{\text{N2}} + \rho g(h_{\text{tank}} - h_{\text{stack,in}}) + \Delta p_{\text{pump}}(u_{\text{pump},i}, \dot{V}_i) - R_{\text{feed}}\dot{V}_i^2 - p_{\text{stack,in},i} \tag{3.16}$$

Since there are two hydraulic circuits, there are the same error measures for both sides, $e_{+,1,i}$, $e_{+,2,i}$ and $e_{+,3,i}$ for the positive electrolyte side, and $e_{-,1,i}$, $e_{-,2,i}$ and $e_{-,3,i}$ for the negative electrolyte side. By summing up the squared error over all measurement points taken for each of the hydraulic circuits and adding the costs for the incorporation of the heights weighted by w_h to bring the terms to similar orders of magnitude, one gets the cost function:

$$\begin{aligned} J(x_{\text{par}}) = &\sum_{i=1}^{N_+}(e_{+,1,i}^2(x_{\text{par}}) + e_{+,2,i}^2(x_{\text{par}}) + e_{+,3,i}^2(x_{\text{par}})) \\ &+ \sum_{i=1}^{N_-}(e_{-,1,i}^2(x_{\text{par}}) + e_{-,2,i}^2(x_{\text{par}}) + e_{-,3,i}^2(x_{\text{par}})) \\ &+ w_h J_h(x_{\text{par}}) \end{aligned} \tag{3.17}$$

Here, the number of measurement points for the positive side is N_+ and the negative side is N_-. This optimization problem could be rewritten as a quadratic program or simply be solved by any unconstrained optimization solver like for example Matlab's fminsearch. Figure 3.8 and 3.9 show the determined model compared to the stationary measurement points for both hydraulic circuits respectively. The model seems to fit to the data quite well, with only small deviations.

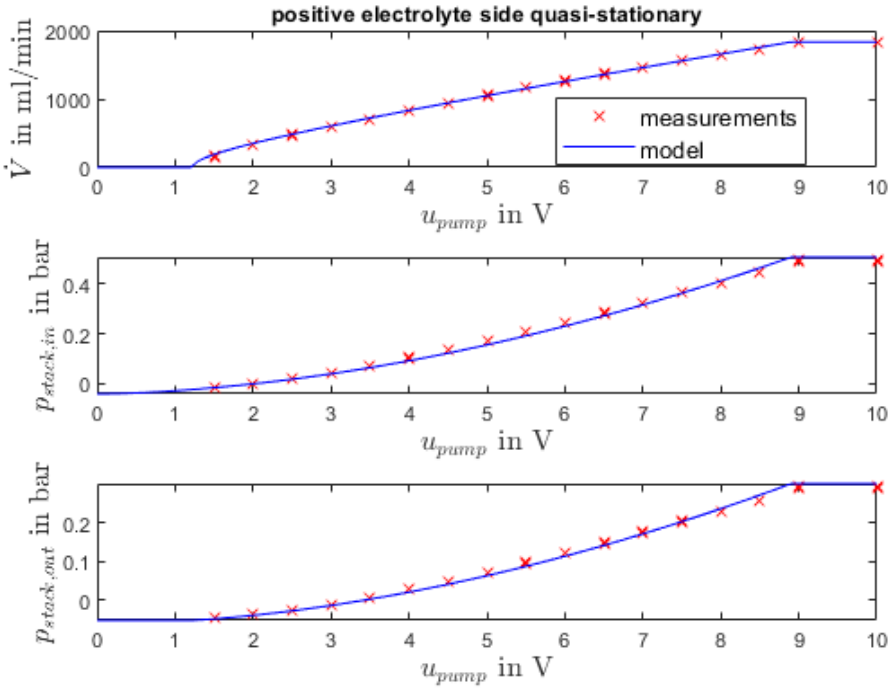

Figure 3.8.: Measurements of the positive electrolyte side compared with the fitted model.

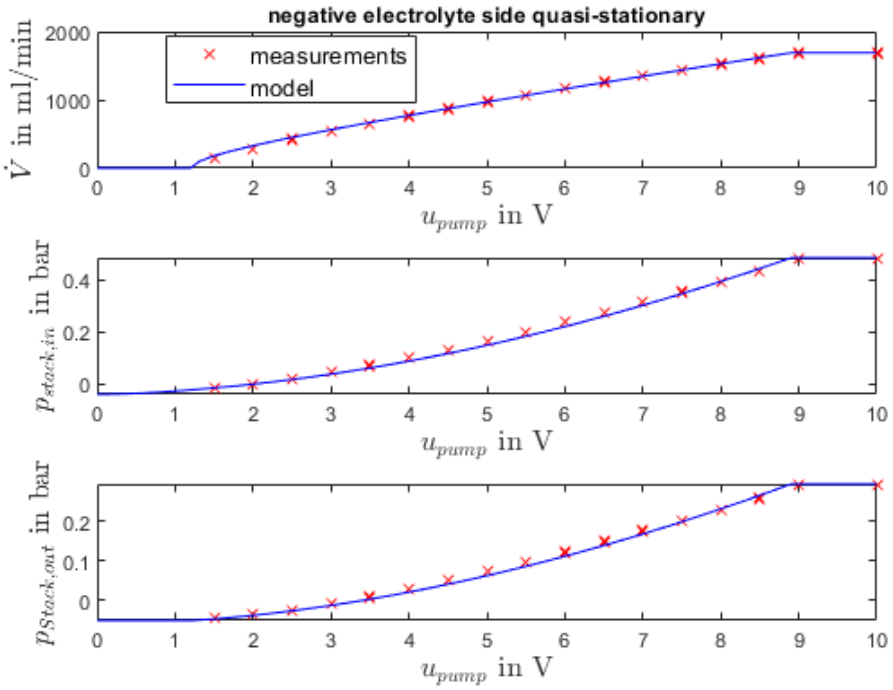

Figure 3.9.: Measurements of the negative electrolyte side compared with the fitted model.

3.1.3. Modelling of the dynamic behaviour of the hydraulic system

To describe the transitions between different steady state operating points $\dot{V}_s$ the modelling of the dynamic behaviour is essential. By considering the inertia of the incompressible fluid and the pump's dynamic characteristics itself, the dynamics of the volume flow $\dot{V}$ can be described as a second order delay element [8]:

$$\dot{V}_s(u_n(t - t_{dead})) = \dot{V} + 2TD\frac{d\dot{V}}{dt} + T^2\frac{d^2\dot{V}}{dt^2} \tag{3.18}$$

The time constant T and the damping constant D are parameters, which can be determined with a least squares approach and the use of an unconstrained solver like for example Matlab's fminsearch. There is also a small dead time in the system t_{dead}, which probably comes from transmission delay on the sensor and actor side. Figure 3.10 shows the fitted dynamic behaviour compared to the measurements and the quasi stationary value for the given control voltage. It can be seen that the dynamic behaviour can be captured quite well.

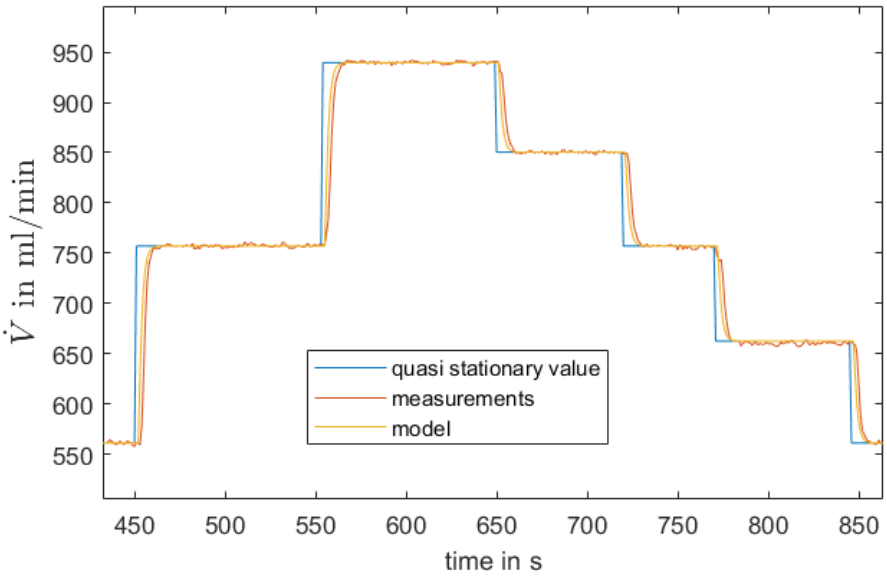

Figure 3.10.: Comparison of measured data with the modelled data.

3.2. Control design and validation

In this section a control structure based on the developed model (section 3.1) is introduced in section 3.2.1. In section 3.2.2 the control structure is tested at the redox flow battery test bench, described in chapter 2.

3.2.1. Control design

There are two goals for the control structure:

- Tracking of the reference volume flow $\dot{V}_{\text{ref}}$
- Avoiding damage to the membrane due to high pressure differences

The first step for the control structure is a static feedforward control, which is developed based on the developed model. By using equation (3.12) and solving for u_n instead of solving for $\dot{V}$, u_n as a function of $\dot{V}$ is obtained:

$$u_n(\dot{V}) = -\frac{\beta\dot{V}}{2\alpha} + \sqrt{\left(\frac{\beta\dot{V}}{2\alpha}\right)^2 - \frac{1}{\alpha}\left(\rho g(h_{\text{tank}} - h_{\text{tank,in}}) - R_{\text{stack,lin}}\dot{V} - R_{\text{ges,quad}}\dot{V}^2\right)} \quad (3.19)$$

This function can be used for the feedforward control action, but one has to calculate back to the real control voltage of the pump u_{pump} using the inverse of the correction function (see equation (3.6)).

$$u_{\text{ff}}(\dot{V}) = [u_n(\dot{V})]^{\frac{1}{0.9}} \quad (3.20)$$

This feedforward control is applied to the side, where the volume flow is measured, which is the positive electrolyte side here. To compensate the effect of model uncertainties, a feedback PI-controller is used. The control error for this PI-controller is the difference of a filtered V_{ref} and the measured volume flow $\dot{V}_+$. The filter uses the plant's dynamic characteristics (see equation (3.18)) and applies it to the reference signal. This filtered signal is for a well determined model a good estimate for the expected measurements, if only the feedforward control action would be applied. So the PI-controller only has to compensate for deviations due to model error.
Because both hydraulic circuits of the system are very similar to one another, the corresponding control signals also have to be very similar. Therefore the control signal of the positive electrolyte side is used as a feedforward control action for the negative electrolyte side.
Because there are no pressure measurements in the stack, the pressure across the membrane can not be measured or controlled directly. But if the pressure difference between the inlets and the pressure difference between the outlets of the stack are small, also the pressure difference across the membrane has to be small. To reduce the variables to control, the flow resistances from the stack outlets to the tank have to be tuned manually with the needle valves, such that a small pressure difference at the inlets also leads to an

small pressure difference at the outlets of the stack. With that tuning, it is enough to only control the pressure difference at the inlets of the stack. The pressure difference between the inlets of the stack is controlled via a second PI controller towards zero. The proposed control structure can be seen in Figure 3.11.

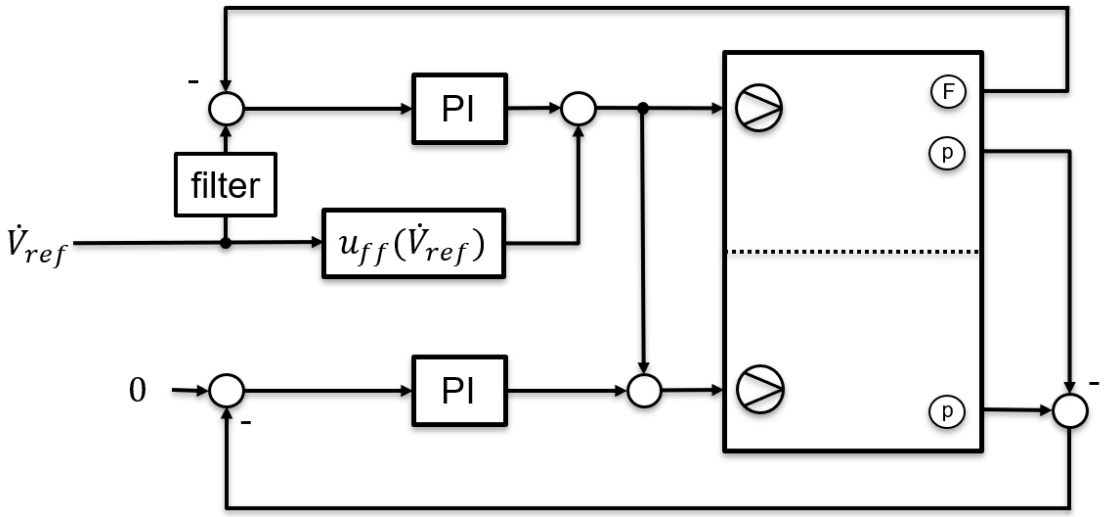

Figure 3.11.: Structure for the control of the hydraulics.

3.2.1.1. Predictive reference limitation

The proposed structure has one weakness. The two hydraulic circuits are not exactly the same. It might happen that the hydraulic circuit responsible for the pressure difference control is weaker, meaning the same control voltage leads to less flow and so less pressure at the inlet of the stack. Since the control voltage for the pumps is limited, it might happen that the hydraulic circuit for pressure difference control goes into saturation first. In this situation, the controller can't regulate the pressure difference anymore. Figure 3.12 shows this effect in the simulation for the determined parameter set. The reference signal for the volume flow hereby is a combination of two step signals and a sinusoidal signal. From 65 seconds to 80 seconds, the pressures at the stack inlets differ a lot.

One easy solution for this problem would be to do the flow tracking with the weaker hydraulic circuit and control the pressure difference with the other one. For this, the flow sensor has to be moved to the other hydraulic circuit. This would be possible for the redox flow test bench, but might not be easily possible in general. Also, the parameters of the system might drift over long time scales due to abrasion and deposit. This could change the system such that the explained condition occurs.
One way to solve this problem, without changing the hardware, is to limit the reference for the volume flow. This is done here by predicting, if the reference will lead to the weaker hydraulic circuit reaching it's limit.
The predictive reference limitation uses the last calculated values of the two PI controllers and the pre-calculated feedforward control action for the reference $\dot{V}_{\mathrm{ref}}$ to predict if the

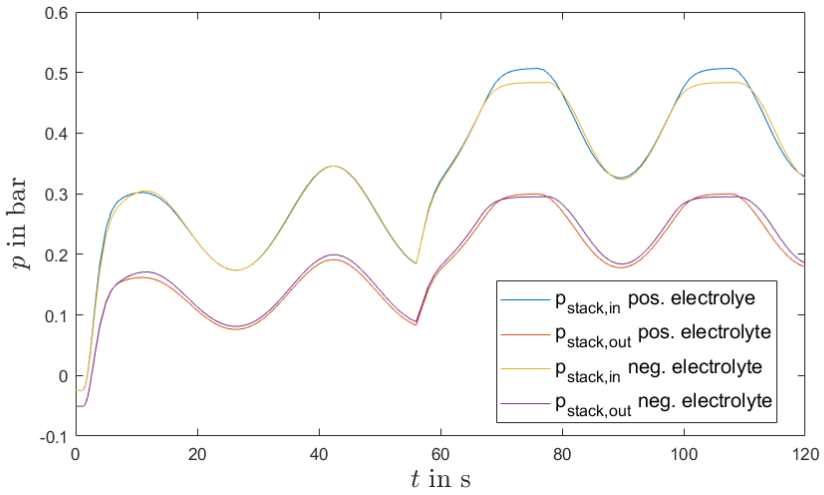

Figure 3.12.: Result of the simulation without reference limitation.

maximal control voltage will be reached. If for a given reference the maximal control voltage is reached, the limit for the reference $\dot{V}_{\text{lim}}$ is lowered until the inequality

$$u_{\text{ff}}(\dot{V}_{\text{lim}}) + u_{\text{PI},\dot{V}} + u_{\text{PI},\Delta p} < u_{\text{max}} - \Delta u_{\text{safe}} \tag{3.21}$$

is fulfilled. Hereby Δu_{safe} is introduced to limit the reference slightly below the actual saturation voltage u_{max} such that there is a small buffer where the PI controller reducing the pressure difference can work. This avoids a big overshoot of the pressure difference for rapid change of the reference.
By limiting the reference signal in this way, the pressure difference can be kept small, as Figure 3.13 shows. The reference signal for the volume flow is the same as in Figure 3.12, but now the limitation hinders the positive electrolyte side to rise to values where the pressure difference can't be controlled anymore. Since the two hydraulic circuits are not

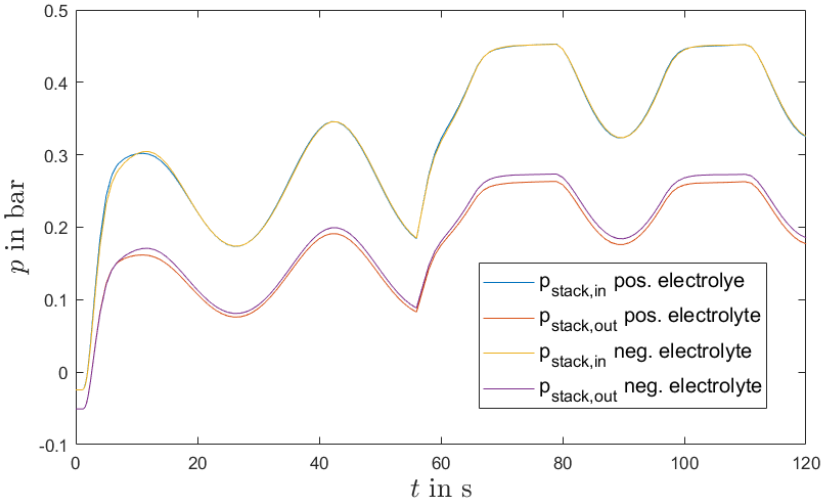

Figure 3.13.: Result for the pressures from simulation with the predictive reference limitation.

exactly identical and only the pressure difference at the inlets of the stack is measured,

the pressure difference at the outlets might not be zero. But by adjustment of the needle valves while operation at a high volume flow the two hydraulic circuits can be matched quite well.

3.2.2. Validation on test bench

For the experiment on the test bench, the settings for the 2 PI controllers in Table 3.1 were used. For delay and filtering of the reference for the volume flow PI controller, the determined dead time was 2s and the system dynamics transfer function discretized by the zero-order-hold method to replicate the sampling behaviour of the data acquisition system was

$$H(z) = \frac{0.2769z + 0.1184}{z^2 - 0.6811z + 0.0765}. \tag{3.22}$$

controller	proportional K_p	integration time T_i
volume flow	$1 \cdot 10^4 \frac{\mathrm{V}}{\mathrm{m^3/s}}$	0,009 min
pressure difference	$-2 \cdot 10^{-5} \frac{\mathrm{V}}{\mathrm{Pa}}$	0,01 min

Table 3.1.: Controller settings for the experiments on the test bench.

By inspection of figure 3.14 it can be seen that the proposed controller fulfils its two objectives. The first one, the tracking of a reference volume flow, can be seen in the upper plot. In the second plot, one can see that the measured pressures at the inlets are close to each other all the time. Since the return pipe flow resistances are matched with the needle valves also the outlet pressures are close to one another.

The volume flow controller was also tested against an ordinary PI-controller parametrized with the T-sum rule and an additional tuning. The parameters of this controller were $K_c = 0.15 \ \frac{\mathrm{V}}{\mathrm{ml/min}}$ and $T_\mathrm{i} = 0,0227$ min. The comparison of the two controllers can be seen in Figure 3.15. Three different step-wise changes of the reference were carried out. It can be seen that the proposed controller follows the reference after the dead time of the system pretty rapidly compared to the PI-controller. It only takes the model-based controller about 4 seconds to reach a value acceptable close to the reference, while the PI-controller takes at least 10 seconds to reach the same values. But in terms of accuracy, the PI-controller is better for some time, when there is a reference step downwards. The reason is that the dynamics of the system do behave slightly different for a pump speed increase than a decrease. This leads to a mismatch in the estimated dynamic parameters and leading to the PI-controller reacting to early to the not yet settled transient behaviour and therefore leading to this transient behaviour of the volume flow.

Figure 3.16 shows the effect of the reference limitation implemented on the test bench. The limitation can be seen in action after t=3525s. Although the pressure difference is hold in tolerable bounds of $\pm$0.02bar, the limitation doesn't work nearly as good as in the simulation. The reason might be that the predictive reference limitation doesn't

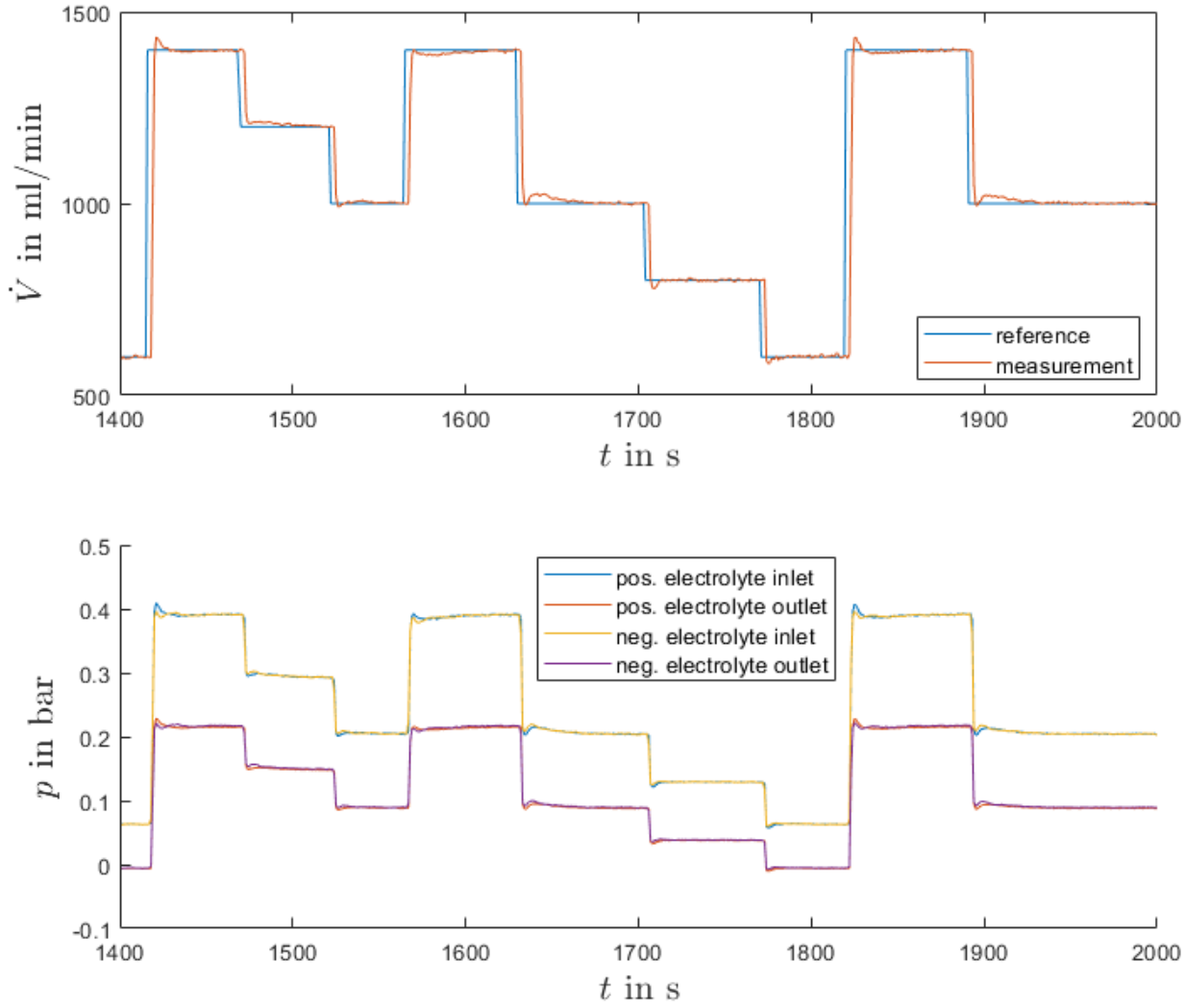

Figure 3.14.: Upper plot shows the reference tracking performance of the proposed controller. The lower plot shows the corresponding pressure measurements at the inlets and outlets.

consider any of the dynamics. The prediction causes a feedback loop, which leads to this oscillating behaviour. To avoid this behaviour a more conservative approach with a fixed limit, determined by slowly increase of the reference volume flow until the first pump reaches their upper limit. The fixed limits will be used instead in the rest of this work and are also suggested to be used if no deposit of the electrolytes is expected.

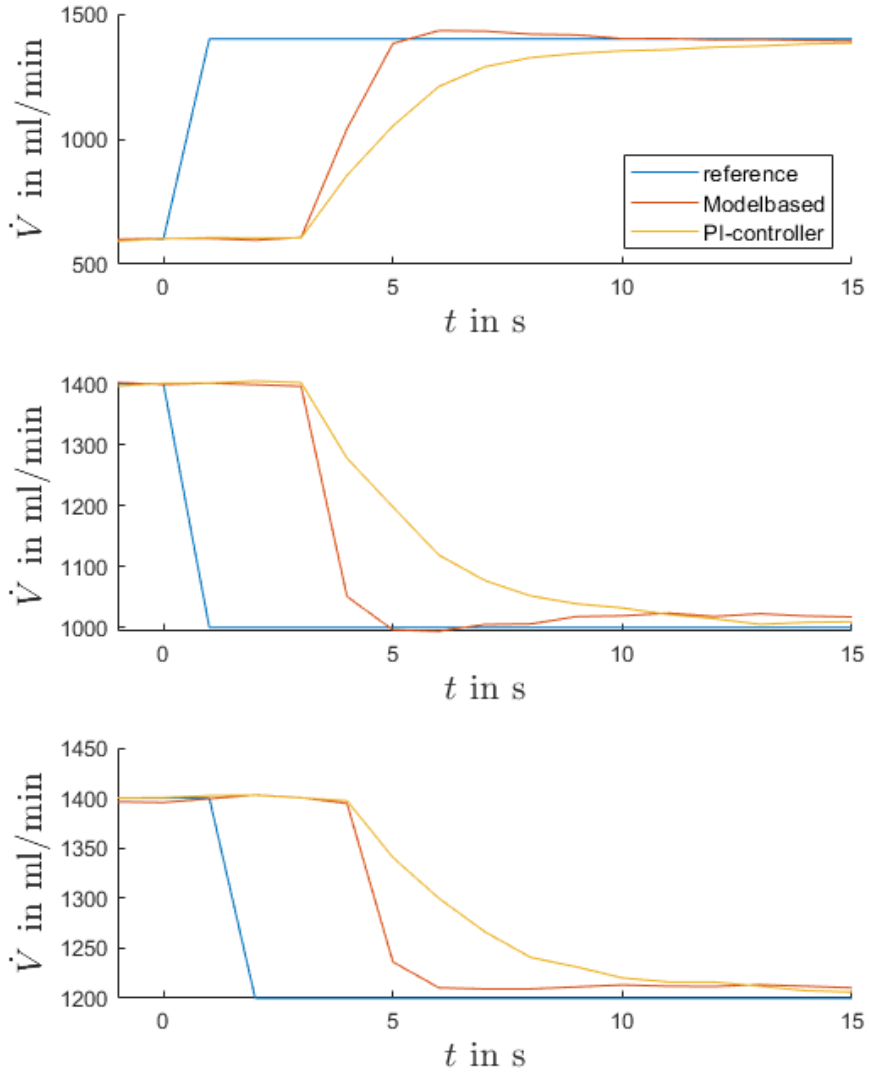

Figure 3.15.: All plots show the plants the response of the plant for a sudden reference change of different heights. The proposed model-based controller was compared to a PI-controller parametrized with the T-sum rule, followed by some fine-tuning.

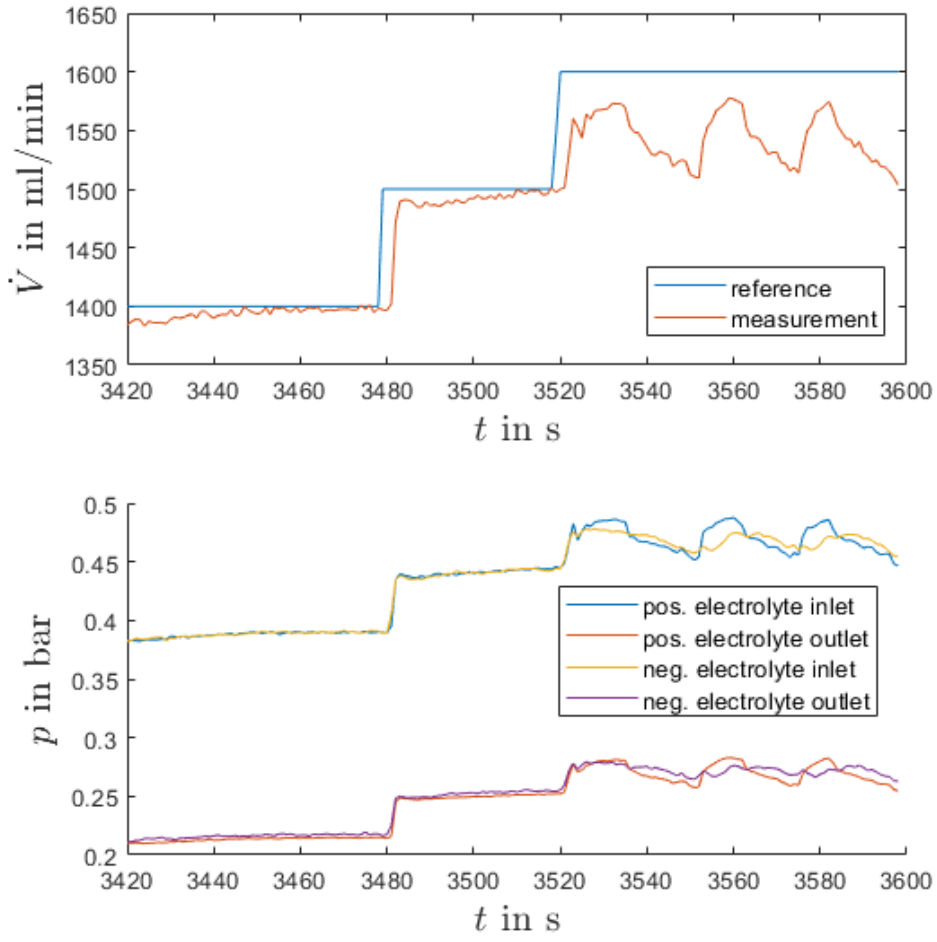

Figure 3.16.: The upper plot shows the volume flow for the reference limitation in action. The lower plot shows the corresponding pressure measurements.

4. Electro-Chemistry

The key process in the investigated redox flow battery are the two redox reactions happening in the cells, either for charging in the one direction or for discharging in the other direction. Hereby anthraquinone-2,6-disulfonate AQDS and anthrahydroquinone-2,6-disulfonate AHQDS are the reactants in the negative electrolyte reaction. The positive electrolyte reactants are methoxyquinonesalt MQS and methoxyhydroquinonesalt MHQS.

$$\text{pos. electrolyte reaction:} \qquad \text{MHQS} \underset{\text{discharge}}{\overset{\text{charge}}{\rightleftarrows}} \text{MQS} + 2H^+ + 2e^- \tag{4.1}$$

$$\text{neg. electrolyte reaction:} \qquad \text{AQDS} + 2H^+ + 2e^- \underset{\text{discharge}}{\overset{\text{charge}}{\rightleftarrows}} \text{AHQDS} \tag{4.2}$$

The H^+ ions hereby are able to diffuse through the membrane, while the electrons have to take their way through the outer electric circuit. These chemical reactions store energy for charging and release it for discharging. To know how much energy is stored in the whole battery the knowledge of the State-of-Charge SOC is important. So the main goal of this chapter is the development of method for the determination of the State-of-Charge SOC, which is not directly measurable. It is defined as

$$\text{SOC} = \frac{Q}{Q_{\text{max}}}, \tag{4.3}$$

where Q is the amount of charging currently stored in the battery and Q_{max} is the maximal storable charge. In theory Q_{max} should be known, due to the amount of redox active substance added in the filling process. But experiments showed, that only about two thirds of the theoretical storable charge are really available directly after the filling of the battery, the reason is not known. Some assumptions could be a limited purity of the redox active substances or oxidation happening while filling of the battery. Additionally the maximal storable charge Q_{max} is decreasing very slowly over time, also here the reason is not known. For this reason, also the determination of Q_{max} is a goal of this chapter.
The SOC and Q_{max} are both associated with the amount of the different species in the electrolytes. Since the redox flow battery consists of two electrolytes, both values can be defined for both electrolytes separately. By the definition of the SOC and Q_{max} for both electrolytes separately it is possible to determine which electrolyte limits the amount which can be charged and discharged and to also describe imbalances between the two electrolytes. So the State-of-Charge and maximal storable charge for the positive electrolyte,

SOC_+ and $Q_{max,+}$, and the negative electrolyte, SOC_- and $Q_{max,-}$, can be defined by:

$$SOC_+ = \frac{c_{MQS,cell} V_{stack} + c_{MQS,tank} V_{tank}}{(c_{MQS,cell} + c_{MHQS,cell}) V_{stack} + (c_{MQS,tank} + c_{MHQS,tank}) V_{tank}} \tag{4.4}$$

$$Q_{max,+} = zF \left[(c_{MQS,cell} + c_{MHQS,cell}) V_{stack} + (c_{MQS,tank} + c_{MHQS,tank}) V_{tank} \right] \tag{4.5}$$

$$SOC_- = \frac{c_{AHQDS,cell} V_{stack} + c_{AHQDS,tank} V_{tank}}{(c_{AHQDS,cell} + c_{AQDS,cell}) V_{stack} + (c_{AHQDS,tank} + c_{AQDS,tank}) V_{tank}} \tag{4.6}$$

$$Q_{max,-} = zF \left[(c_{AHQDS,cell} + c_{AQDS,cell}) V_{stack} + (c_{AHQDS,tank} + c_{AQDS,tank}) V_{tank} \right] \tag{4.7}$$

Hereby $c_{i,cell}$ and $c_{i,tank}$ are the concentrations in $\frac{mol}{m^3}$ of the i-th species in the cells and tank assuming perfect mixing with the volume of all the cells combined V_{stack} and the tank volume V_{tank}. Electrolyte in the pipes here is considered negligible compared to the tank and stack volumes or can be seen as an tank extension. The number of electrons participating in the reaction $z = 2$ and the Faraday constant F link the amount of redox active substance to the corresponding charge according to Faraday's law of electrolysis. So for known concentrations, it would be possible to calculate the SOC and Q_{max} for both electrolytes, but the concentrations can also not be measured directly. Therefore in section 4.1 a model is developed, which describes the evolution of these concentrations and their effect on the measurements taken by the redox probes and cell voltage measurement. This model is parametrized using experimental data in section 4.2. Based on this parametrized model, a nonlinear state observer from literature is adapted to estimate these concentrations in section 4.3.

4.1. Modelling of the electro-chemical behaviour

There are different models describing redox flow batteries already developed, mainly specifically for all-vanadium flow batteries. Three different model categories describing the behaviour of redox flow batteries can be found in literature, namely equivalent circuit systems, distributed parameter systems and lumped parameter systems [9]. Distributed parameter systems are computational intense and quite complex. They deliver a more detailed spacial distribution of the concentrations, which is useful for design purposes. But the complexity in combination with real-time operation is not suited for control purposes. Equivalent circuit models, which describe the behaviour of the battery by an equivalent electric circuit with different ideal components, do not allow a detailed look at the underlying chemical processes and are therefore not useful to determine the wanted concentrations. Lumped parameter systems are a good compromise between model complexity, accuracy and insight into the underlying chemistry. So the model developed here will be a lumped parameter model, using only the concentrations in the tanks and the stack. This assumes that the electrolytes in the tank and the stack are perfectly mixed. The ideal assumption, that only H^+ ions can diffuse through the membrane, doesn't hold in reality. Instead also molecules of the redox active substances diffuse through the membrane, but at a very slow base. How fast this happens and what

reactions happen after the diffusion is not known at the moment and and thus content of current fundamental research. Due to this missing knowledge about the diffusion through the membrane and the resulting reactions of the electrolytes, the diffusion of reactants through the membrane is neglected in this work. Instead, all losses are considered to be losses due to shunt currents, which are modelled first, in section 4.1.1. Based on the underlying chemical reactions of the electrolytes in equation (4.1) and (4.2) a model describing the temporal evolution of the concentrations is developed in section 4.1.2. The concentration dependence of the redox potentials measurements at the redox probes is modelled in section 4.1.3. The modelling of the cell voltage is done in 4.1.4.

4.1.1. Modelling of shunt currents

Shunt currents are parasitic currents due to the structure of battery stacks of a flow battery. A schematic depiction of the stack structure can be seen in figure 4.1, which illustrates the flow of these shunt currents. The electrolytes are pumped into the stack, where they are distributed to the individual cells. The return flows of all the cells join again after getting pumped through the cell. This hydraulic parallel structure in combination with the non-zero conductivity of the electrolytes leads to electrically conducting paths from one cell to all the other cells over the electrolyte filled channels and manifolds for shunt currents to flow and to continuously discharge the battery.
To minimize these shunt currents, the channels between the cells and the distribution or collection pipes are designed to increase the effective path length and therefore increase the ohmic resistance linked to these channels. For example, the stack of the test bench used, see chapter 2, has serpentine like channels.

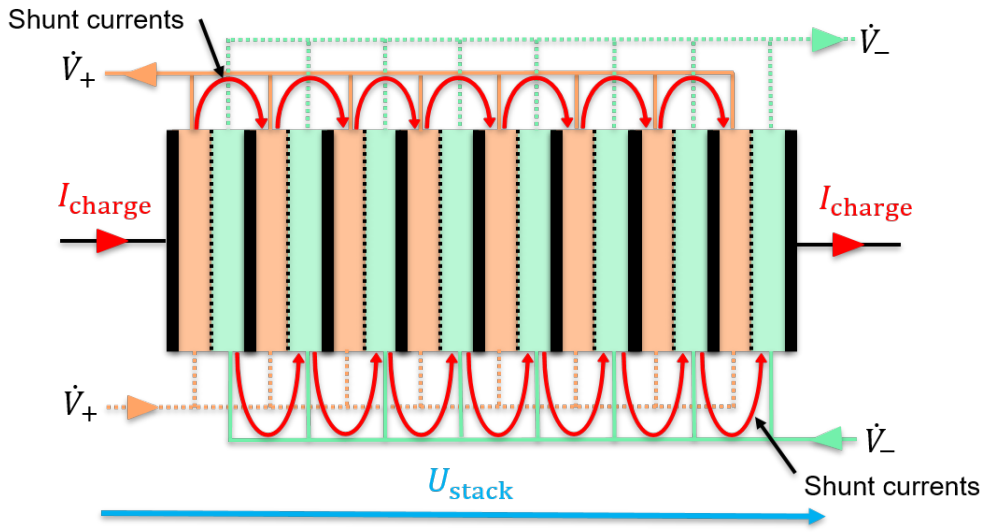

Figure 4.1.: Schematic depiction of the battery stack showing how the hydraulic parallel structure of the 8 cells leads to parasitic paths for shunt currents to flow.

To model the effects of these shunt currents different approaches are used in literature. One way is to use an electrical circuit diagram with resistances corresponding to channels, manifolds and cells, e.g. [10]. This approach allows to distinguish the different shunt

currents from cell to cell, but at the cost of a lot of unknown model parameters. Therefore in this thesis the effects of shunt currents are considered by one equivalent resistance R_{loss} in parallel to the stack, causing a parasitic current I_{loss}, proportional to the stack voltage U_{stack}, discharging the battery:

$$I_{\text{loss}} = \frac{U_{\text{stack}}}{R_{\text{loss}}} \tag{4.8}$$

The underlying assumption here is that the overall effect of the shunt currents is linear with the stack voltage U_{stack}.

4.1.2. Modelling of the temporal evolution of the concentrations

The temporal evolution of the concentrations in the cells is based on the two basic electrochemical reactions in the equations (4.1) and (4.2). The reactions either happen in one or the other direction, which is linked to the direction the current is flowing.

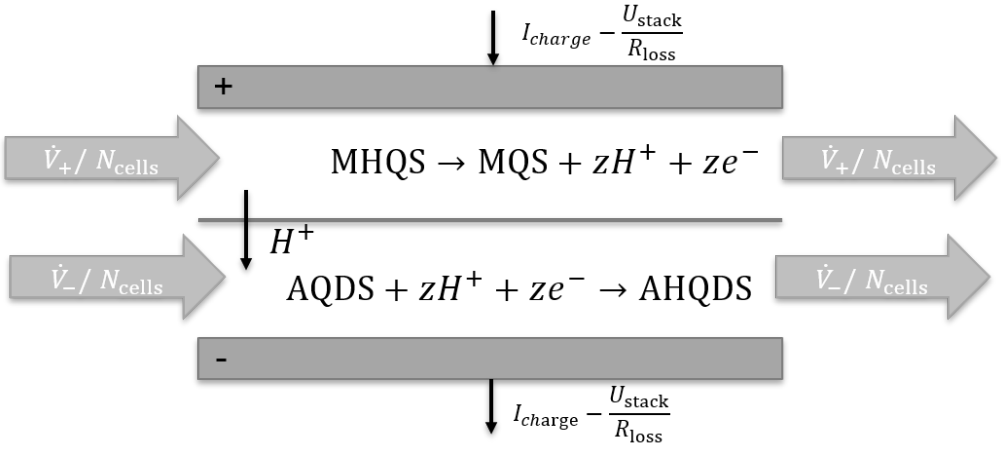

Figure 4.2.: Schematic depiction of the charge process in one cell of the battery stack.

Figure 4.2 depicts one single cell of the stack, consisting out of two half cells containing the two different electrolytes in it. Due to an applied cell voltage a positive charging current I_{charge} is flowing. The shunt current losses are considered with the term $-\frac{U_{\text{stack}}}{R_{\text{loss}}}$ according to equation (4.8). Assuming no electrolyte flow through the cell, the rate of change of the amount of the different species in the respective half cell $\frac{dn_{i,\text{cell}}}{dt}$, for $i \in \{\text{MHQS, MQS, AQDS, AHQDS}\}$ is proportional to the current. It can be expressed

according to the chemical reaction equations and Faraday's law of electrolysis, with:

$$\frac{dn_{\mathrm{MQS,cell}}}{dt} = \frac{\left(I_{\mathrm{charge}} - \frac{U_{\mathrm{stack}}}{R_{\mathrm{loss}}}\right)}{zF} \tag{4.9}$$

$$\frac{dn_{\mathrm{MHQS,cell}}}{dt} = -\frac{\left(I_{\mathrm{charge}} - \frac{U_{\mathrm{stack}}}{R_{\mathrm{loss}}}\right)}{zF} \tag{4.10}$$

$$\frac{dn_{\mathrm{AHQDS,cell}}}{dt} = \frac{\left(I_{\mathrm{charge}} - \frac{U_{\mathrm{stack}}}{R_{\mathrm{loss}}}\right)}{zF} \tag{4.11}$$

$$\frac{dn_{\mathrm{AQDS,cell}}}{dt} = -\frac{\left(I_{\mathrm{charge}} - \frac{U_{\mathrm{stack}}}{R_{\mathrm{loss}}}\right)}{zF} \tag{4.12}$$

Here, z is the number of electrons transferred per reaction, which are two electrons for both of the given reactions. The Faraday constant $F = 96485\mathrm{Asmol}^{-1}$ is linking the amount of substance of single charged ions to the corresponding charge.
By further considering the volume flow through the cell $\frac{\dot{V}_{\pm}}{N_{\mathrm{cells}}}$, one gets:

$$\frac{dn_{\mathrm{MQS,cell}}}{dt} = \frac{\dot{V}_{+}}{N_{\mathrm{cells}}}\left(c_{\mathrm{MQS,tank}} - c_{\mathrm{MQS,cell}}\right) + \frac{\left(I_{\mathrm{charge}} - \frac{U_{\mathrm{stack}}}{R_{\mathrm{loss}}}\right)}{zF} \tag{4.13}$$

$$\frac{dn_{\mathrm{MHQS,cell}}}{dt} = \frac{\dot{V}_{+}}{N_{\mathrm{cells}}}\left(c_{\mathrm{MHQS,tank}} - c_{\mathrm{MHQS,cell}}\right) - \frac{\left(I_{\mathrm{charge}} - \frac{U_{\mathrm{stack}}}{R_{\mathrm{loss}}}\right)}{zF} \tag{4.14}$$

$$\frac{dn_{\mathrm{AHQDS,cell}}}{dt} = \frac{\dot{V}_{-}}{N_{\mathrm{cells}}}\left(c_{\mathrm{AHQDS,tank}} - c_{\mathrm{AHQDS,cell}}\right) + \frac{\left(I_{\mathrm{charge}} - \frac{U_{\mathrm{stack}}}{R_{\mathrm{loss}}}\right)}{zF} \tag{4.15}$$

$$\frac{dn_{\mathrm{AQDS,cell}}}{dt} = \frac{\dot{V}_{-}}{N_{\mathrm{cells}}}\left(c_{\mathrm{AQDS,tank}} - c_{\mathrm{AQDS,cell}}\right) - \frac{\left(I_{\mathrm{charge}} - \frac{U_{\mathrm{stack}}}{R_{\mathrm{loss}}}\right)}{zF} \tag{4.16}$$

This assumes equal distribution of the volume flow among all cells, which should be approximately true for a properly designed stack. Here N_{cells} is the number of cells in the stack and $c_{i,\mathrm{cell}}$ and $c_{i,\mathrm{tank}}$, for $i \in \{\mathrm{MHQS, MQS, AQDS, AHQDS}\}$, are the concentrations of the species in cell and tank, respectively. The concentrations can be expressed by:

$$c_{i,\mathrm{cell}} = \frac{n_{i,\mathrm{cell}}}{\varepsilon_{\mathrm{por}} V_{\mathrm{cell}}} \tag{4.17}$$

$$c_{i,\mathrm{tank}} = \frac{n_{i,\mathrm{tank}}}{V_{\mathrm{tank}}} \tag{4.18}$$

Here V_{tank} is the volume of the electrolyte in the tank, V_{cell} is the volume of one half cell, determined from design plans of the stack, and $\varepsilon_{\mathrm{por}}$ accounts for the porosity of the carbon felts in the cells, which leaves less space in the half cell for the electrolyte. $\varepsilon_{\mathrm{por}}$ is a parameter, to be determined by experiments.
It is assumed in this work, that all the cells have the same concentration of species and are described in the same way. This can also be interpreted that all cells behave like an

averaged cell. By combining equation (4.17) with equations (4.13)-(4.16) one gets

$$V_{\text{stack}} \frac{dc_{\text{MQS,cell}}}{dt} = \dot{V}_+ \left(c_{\text{MQS,tank}} - c_{\text{MQS,cell}}\right) + \frac{\left(I_{\text{charge}} - \frac{U_{\text{stack}}}{R_{\text{loss}}}\right) N_{\text{cells}}}{zF} \tag{4.19}$$

$$V_{\text{stack}} \frac{dc_{\text{MHQS,cell}}}{dt} = \dot{V}_+ \left(c_{\text{MHQS,tank}} - c_{\text{MHQS,cell}}\right) - \frac{\left(I_{\text{charge}} - \frac{U_{\text{stack}}}{R_{\text{loss}}}\right) N_{\text{cells}}}{zF} \tag{4.20}$$

$$V_{\text{stack}} \frac{dc_{\text{AHQDS,cell}}}{dt} = \dot{V}_- \left(c_{\text{AHQDS,tank}} - c_{\text{AHQDS,cell}}\right) + \frac{\left(I_{\text{charge}} - \frac{U_{\text{stack}}}{R_{\text{loss}}}\right) N_{\text{cells}}}{zF} \tag{4.21}$$

$$V_{\text{stack}} \frac{dc_{\text{AQDS,cell}}}{dt} = \dot{V}_- \left(c_{\text{AQDS,tank}} - c_{\text{AQDS,cell}}\right) - \frac{\left(I_{\text{charge}} - \frac{U_{\text{stack}}}{R_{\text{loss}}}\right) N_{\text{cells}}}{zF} \tag{4.22}$$

with $V_{\text{stack}} = N_{\text{cells}} \varepsilon_{\text{por}} V_{\text{cell}}$. The concentrations in the tanks can be described in a similar way:

$$V_{\text{tank}} \frac{dc_{i,\text{tank}}}{dt} = \dot{V}_\pm \left(c_{i,\text{cell}} - c_{i,\text{tank}}\right) \quad \text{, for } i \in \{\text{MHQS, MQS, AQDS, AHQDS}\} \tag{4.23}$$

By summarizing the cell concentrations and the tank concentrations in one state vector

$$\mathbf{x} = \begin{bmatrix} c_{\text{MQS,cell}} \\ c_{\text{MHQS,cell}} \\ c_{\text{AHQDS,cell}} \\ c_{\text{AQDS,cell}} \\ c_{\text{MQS,tank}} \\ c_{\text{MHQS,tank}} \\ c_{\text{AHQDS,tank}} \\ c_{\text{AQDS,tank}} \end{bmatrix} \tag{4.24}$$

the equations can be expressed by the following dynamic system:

$$\frac{d}{dt}\mathbf{x} = \begin{bmatrix} \frac{-\dot{V}_+}{V_{\text{stack}}} & 0 & 0 & 0 & \frac{\dot{V}_+}{V_{\text{stack}}} & 0 & 0 & 0 \\ 0 & \frac{-\dot{V}_+}{V_{\text{stack}}} & 0 & 0 & 0 & \frac{\dot{V}_+}{V_{\text{stack}}} & 0 & 0 \\ 0 & 0 & \frac{-\dot{V}_-}{V_{\text{stack}}} & 0 & 0 & 0 & \frac{\dot{V}_-}{V_{\text{stack}}} & 0 \\ 0 & 0 & 0 & \frac{-\dot{V}_-}{V_{\text{stack}}} & 0 & 0 & 0 & \frac{\dot{V}_-}{V_{\text{stack}}} \\ \frac{\dot{V}_+}{V_{\text{tank}}} & 0 & 0 & 0 & \frac{-\dot{V}_+}{V_{\text{tank}}} & 0 & 0 & 0 \\ 0 & \frac{\dot{V}_+}{V_{\text{tank}}} & 0 & 0 & 0 & \frac{-\dot{V}_+}{V_{\text{tank}}} & 0 & 0 \\ 0 & 0 & \frac{\dot{V}_-}{V_{\text{tank}}} & 0 & 0 & 0 & \frac{-\dot{V}_-}{V_{\text{tank}}} & 0 \\ 0 & 0 & 0 & \frac{\dot{V}_-}{V_{\text{tank}}} & 0 & 0 & 0 & \frac{-\dot{V}_-}{V_{\text{tank}}} \end{bmatrix} \mathbf{x} + \frac{N_{\text{cells}}}{zFV_{\text{stack}}} \begin{bmatrix} 1 \\ -1 \\ 1 \\ -1 \\ 0 \\ 0 \\ 0 \\ 0 \end{bmatrix} \left(I_{\text{charge}} - \frac{U_{\text{stack}}}{R_{\text{loss}}}\right) \tag{4.25}$$

This dynamic model now describes the temporal evolution of the concentrations depending on the volume flow and the charging current. To derive now a full dynamic model describing, the outputs of the system have to be modelled, which are the measurements taken. So the next step is to link this concentrations to the measurements taken at the redox probes and the cell voltage, which will be done in section 4.1.3 for the redox probes and in section 4.1.4 for the cell voltage respectively.

4.1.3. Modelling of the potentials measured by the redox probes

Different concentrations of the redox active species in the electrolytes result into different electro-chemical potentials or also called redox potentials. These potentials are measurable with respect to a reference electrode. The redox potentials for redox flow battery test bench, see chapter 2, are measured by redox probes, which use an Ag/AgCl reference electrode. To describe these measured potentials typically Nernst's equation is used. It links the concentration of the redox active substances to the measured potential. Due to the location of the redox probes the relevant concentrations for modelling are the concentrations in the tanks. For the potential at the redox probe of the negative-side electrolyte E_- Nernst's equation is

$$E_- = E_{0-} + \frac{RT}{zF} \ln\left(\frac{c_{AQDS,\,\text{tank}}}{c_{AHQDS,\,\text{tank}}}\right) = E_{0-} + \frac{RT}{zF} \ln\left(\frac{x_8}{x_7}\right) \tag{4.26}$$

as an expression of our state variables. Here $R = 8.314 \frac{J}{molK}$ is the universal gas constant, T is the temperature of the electrolyte in Kelvin and E_{0-} is the formal potential of the negative-side electrolyte, which corresponds to the value measured for equal concentrations $c_{AHQDS,\,\text{tank}} = c_{AQDS,\,\text{tank}}$.
The potential for the redox probe of the positive-side electrolyte E_+ is described by

$$E_+ = E_{0+} + \frac{RT}{zF} \ln\left(\frac{c_{MQS,\,\text{tank}}}{c_{MHQS,\,\text{tank}}}\right) = E_{0+} + \frac{RT}{zF} \ln\left(\frac{x_5}{x_6}\right) \tag{4.27}$$

with the formal potential E_{0+} for the positive-side electrolyte. E_{0+} and E_{0-} are unknown model parameters to be determined, see section 4.2.1.1. Unfortunately the redox probes tend to drift slowly over time and therefore recalibration is needed frequently, approximately every month.
So these two output equations for our dynamic system linking our state variables the different concentrations to the redox potential measurements.

4.1.4. Modelling of the cell voltages

Another measurement which can be described as an output to the dynamic system is the cell voltage U_{cell}. To be more precise here the averaged cell voltage derived from the stack voltage U_{stack} and number of cells N_{cells} is considered here:

$$U_{\text{cell}} = \frac{U_{\text{stack}}}{N_{\text{cells}}} \tag{4.28}$$

Given that there is no external electric circuit attached, so the electric current flowing through the cell is zero, the cell voltage settles at the so called Open-Circuit-Voltage U_{OCV}. Section 4.1.4.1 describes the modelling of the Open-Circuit-Voltage.
Now for the current I_{charge} flowing through the cell the cell voltage deviates from the Open-Circuit-Voltage by the so called overpotentials η:

$$U_{\text{cell}} = U_{\text{OCV}} + \eta \tag{4.29}$$

Overpotentials η describe the difference between the cell voltage U_{cell} and the Open-Ciruit-Voltage U_{OCV}, when current is flowing. For charging the overpotentials are positive $\eta > 0V$ and for discharge they are negative $\eta < 0V$. For redox flow batteries three kinds of overpotentials are relevant, namely ohmic, activation and concentration overpotentials. The sum of them leads to the total overpotentials η.

$$\eta = \eta_{\text{ohm}} + \eta_{\text{act}} + \eta_{\text{con}} \tag{4.30}$$

The modelling of ohmic overpotentials is described in section 4.1.4.2, the modelling of activation overpotentials in section 4.1.4.3 and the modelling of concentration overpotentials in section 4.1.4.4.

4.1.4.1. Open-Circuit-Voltage

For calculation of the Open-Circuit-Voltage U_{OCV} the redox potentials of the two electrolytes in their corresponding half cell can be used. The positive half cell potential $E_{+,\text{cell}}$ and the negative half cell potential $E_{\text{-,cell}}$ can also be computed by Nernst's equation:

$$E_{+,\text{cell}} = E_{0+} + \frac{RT}{zF} \ln\left(\frac{c_{\text{MQS,cell}}}{c_{\text{MHQS,cell}}}\right) \tag{4.31}$$

$$E_{\text{-,cell}} = E_{0-} + \frac{RT}{zF} \ln\left(\frac{c_{\text{AHQDS,cell}}}{c_{\text{AQDS,cell}}}\right) \tag{4.32}$$

Here E_{0+} and E_{0-} are the positive and negative electrolytes formal potentials with respect to an Ag/AgCl-electrode reference. Here again R is the universal gas constant, T is the absolute temperature of the electrolyte, z is the number of electrons transferred per reaction and F is Faraday's constant.
Following electrochemical theory the Open-Circuit-Voltage is expressed by the difference between the two half cell potentials. Hereby the potential of the reference electrode, implicitly contained in the formal potentials, gets cancelled out. So for no electric current flowing and pumping the electrolytes for long enough time through the stack, the concentrations in tank and stack should be the same and therefore the difference between the redox probe measurements should be equal to the measured Open-Circuit-Voltage. However, in the conducted measurements for different States-of-Charge showed, that there is a linearity error between the Open-Circuit-Voltage calculated from the redox probes and the one measured in the cell, which can be seen in Figure 4.3. The plot shows data points picked from two experiments, where the battery is stepwise discharged or charged followed by some time with zero current, and a line fitted into the data points. The Open-Circuit-Voltage OCV measured in the cell is plotted over the OCV from the difference redox probe measurements. Appendix A.4 explains the conducted stepwise charge and discharge experiments in more detail.

The reason for this linearity error is not clear entirely, but it might have to do with not ideal properties of the reference electrodes and that the electrode properties differ between the cells carbon felt electrodes and the redox probes.

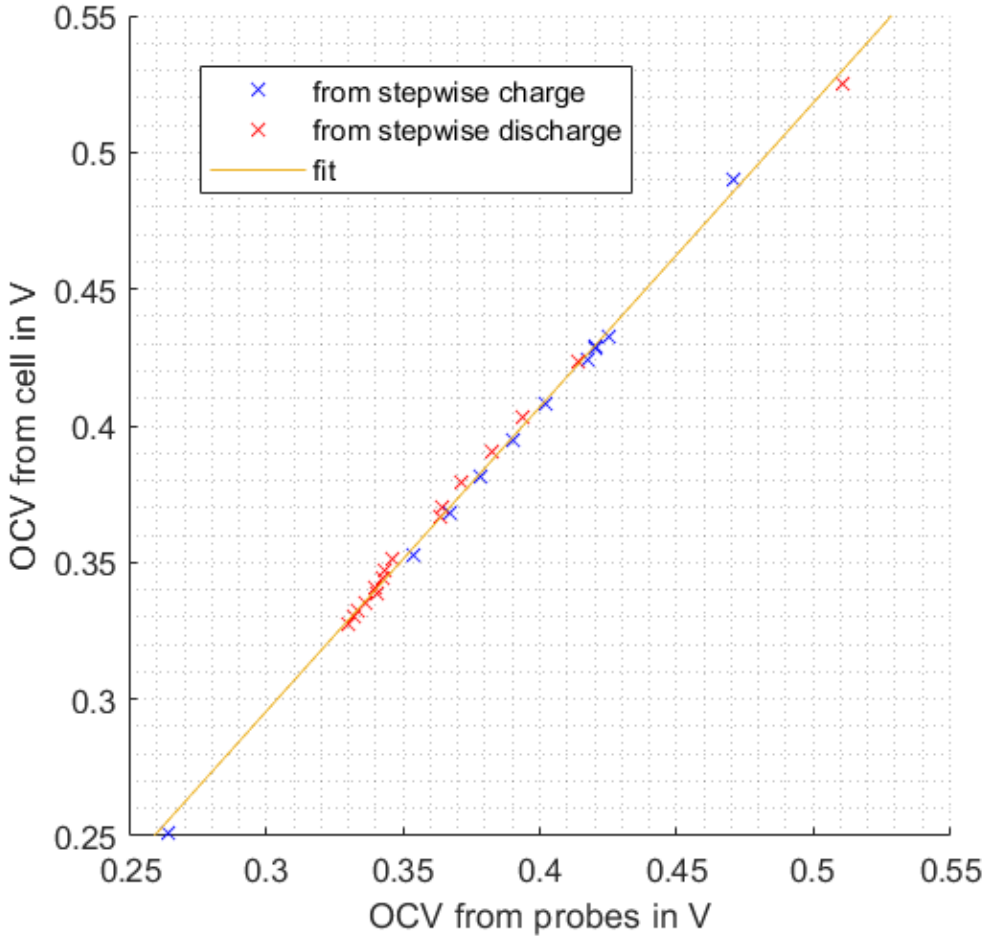

Figure 4.3.: Linear relationship between the OCV of the probes and the OCV measured in the cell.

To compensate for this linearity error, the correction can be done by using the equation of the line fitted to the data points to calculate the Open-Circuit-Voltage U_{OCV}:

$$U_{\mathrm{OCV}} = k_{\mathrm{OCV}} \left[E_{+,\mathrm{cell}} - E_{-,\mathrm{cell}} \right] + d_{\mathrm{OCV}} \tag{4.33}$$

Here k_{OCV} is the slope correction parameter and d_{OCV} corrects for the offset. Both parameters are determined by linear regression of the measurement data.
So by inserting the half cell potentials and the state variables, the Open-Circuit-Voltage can be computed by:

$$U_{\mathrm{OCV}} = k_{\mathrm{OCV}} \left[E_{0+} - E_{0-} + \frac{RT}{zF} \ln \left(\frac{x_1}{x_2} \frac{x_3}{x_4} \right) \right] + d_{\mathrm{OCV}} \tag{4.34}$$

So the Open-Circuit-Voltage, which is the cell voltage for no electric current flowing, can now be linked to the state variables. The following sections now consider the effects of current flowing through the cell, the different overpotentials.

4.1.4.2. Ohmic overpotential

The ohmic overpotential, or also often the ohmic losses, includes all internal ohmic losses of the cell, like the resistance of the electrodes, the electrolyte and the membrane. This different resistances are lumped here into one resistance, describing the total ohmic behaviour of the cell. Some studies indicate that the resistances might change over time and also differ between charging and discharging [11]. For simplicity the ohmic overpotential η_{ohm} are modelled here only to be different for charging and discharging. So the ohmic overpotential is calculated by

$$\eta_{\text{ohm}} = \begin{cases} R_{\text{charge}} \cdot I_{\text{charge}} & \text{for } I_{\text{charge}} \geq 0 \\ R_{\text{discharge}} \cdot I_{\text{charge}} & \text{for } I_{\text{charge}} < 0 \end{cases} \tag{4.35}$$

with the charging resistance R_{charge} and discharge resistance $R_{\text{discharge}}$.

4.1.4.3. Activation overpotential

The activation overpotential is the overpotential required to overcome the activation energy at an electrode for the redox reaction to happen, producing a given current. So basically for both electrodes a separate activation overpotential has to be overcome. The activation overpotentials are typically described by the Butler-Volmer equation, which is an implicit function linking the activation overpotential to the flowing current density at each electrode.
Starting with the positive electrode overpotential $\eta_{\text{act},+}$ the Butler-Volmer equation looks like that:

$$I_{\text{charge}} = I_{0,+} \left[\exp\left(\frac{(1-\alpha_+)zF}{RT} \eta_{\text{act},+} \right) - \exp\left(\frac{-\alpha_+ zF}{RT} \eta_{\text{act},+} \right) \right] \tag{4.36}$$

The charge transfer coefficient α_+ models the asymmetry of the speed between reaction directions, charging or discharging reaction, at the electrode. The so called exchange current $I_{0,+}$ is in general depending on the used electrode and is depending on the concentrations of the reactants in the electrolyte. This concentration dependence is modelled here by:

$$I_{0,+} = zFA_{\text{e}}\, k_{0,+}\, c_{MQS,\text{cell}}^{1-\alpha_+}\, c_{\text{MHQS,cell}}^{\alpha_+} = zFA_{\text{e}}\, k_{0,+}\, x_1^{1-\alpha_+}\, x_2^{\alpha_+} \tag{4.37}$$

Here A_{e} is the effective electrode area and $k_{0,+}$ is the standard rate constant. This concentration dependence is modelled here similar to the expression for one electron processes in [12].
Due to the implicit character of the Butler-Volmer equation, solving for the positive electrode activation overpotential $\eta_{\text{act},+}$ is quite time-consuming and therefore disadvantageous for usage in parameter estimation problems. To avoid this problem here, a function approximation is used to calculate the activation overpotential at the positive electrode.

$$\eta_{\text{act},+} = \begin{cases} \frac{RT}{(1-\alpha_+)zF} \sinh^{-1}\left(\frac{I_{\text{charge}}}{2I_{0,+}} \right) & I_{\text{charge}} \geq 0 \\ \frac{RT}{\alpha_+ zF} \sinh^{-1}\left(\frac{I_{\text{charge}}}{2I_{0,+}} \right) & I_{\text{charge}} < 0 \end{cases} \tag{4.38}$$

Figure 4.4 shows the Butler-Volmer equation and the used approximation in one plot for several different symmetry factors α_+. The approximation shows only small deviations from the correct solution, which legitimises using it instead of the Butler-Volmer equation.

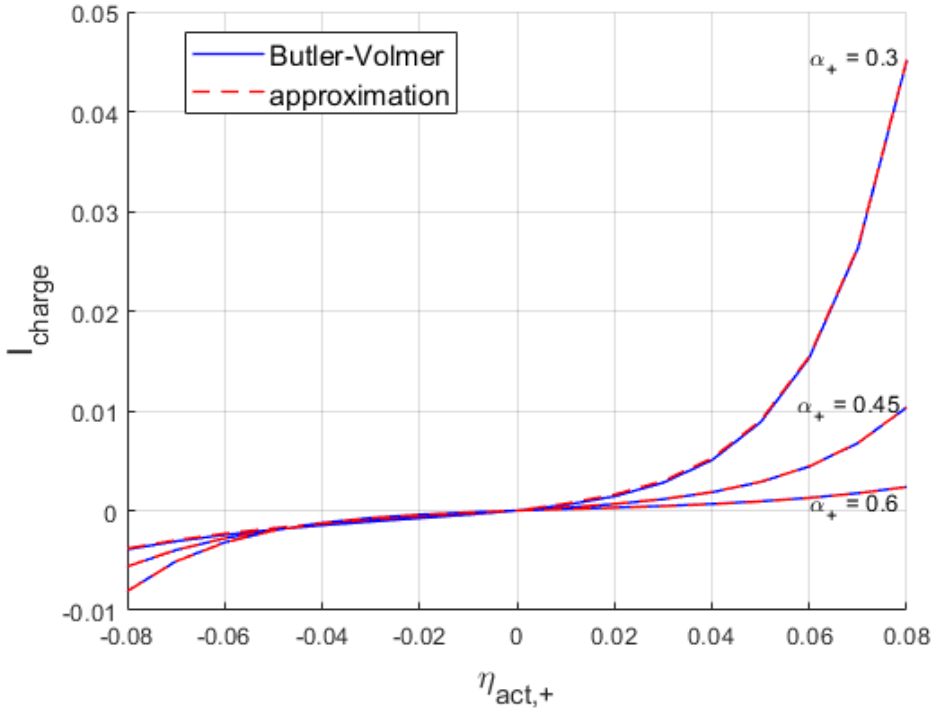

Figure 4.4.: Charging current I_{charge} over the applied activation overpotential $\eta_{act,+}$ for different values of the symmetry factor α_+ to compare Butler-Volmer equation with the proposed approximation in equation (4.38).

The activation overpotential for the negative electrode can be described similarly. The only thing to consider is that the direction of the charging current points in the opposite direction to the assumed current direction in the Butler-Volmer equation, so one gets the equation

$$-I_{charge} = I_{0,-}\left[\exp\left(\frac{(1-\alpha_-)zF}{RT}\eta_{act,-}\right) - \exp\left(\frac{-\alpha_- zF}{RT}\eta_{act,-}\right)\right] \tag{4.39}$$

with the corresponding charge transfer coefficient α_- and the exchange current calculated by

$$I_{0,-} = zFA_e\, k_{0,-}\, c_{AQDS,cell}^{1-\alpha_-}\, c_{AHQDS,cell}^{\alpha_-} = zFA_e\, k_{0,-}\, x_4^{1-\alpha_-} x_3^{\alpha_-} \tag{4.40}$$

By using the same approximation as in equation (4.38) one gets:

$$\eta_{act,-} = \begin{cases} \frac{RT}{(1-\alpha_-)zF}\sinh^{-1}\left(\frac{-I_{charge}}{2I_{0,-}}\right) & I_{charge} < 0 \\ \frac{RT}{\alpha_- zF}\sinh^{-1}\left(\frac{-I_{charge}}{2I_{0,-}}\right) & I_{charge} \geq 0 \end{cases} \tag{4.41}$$

The total activation overpotential η_{act} can now be computed by:

$$\eta_{act} = \eta_{act,+} - \eta_{act,-} \tag{4.42}$$

Note that the activation overpotential of the negative side has to be considered here with a minus, because of the definition of the current and overpotential direction for the Butler-Volmer-equation.

4.1.4.4. Concentration overpotential

Concentration overpotentials are also called transport overpotentials. They are linked to the transport limitation of reactants from the bulk electrolyte to the electrode surface [13], where the reactions happen. They get dominant if the current converts the reactants faster than they can be delivered to the electrode, which is the case for high currents, low concentrations of the reactants or the volume flow of the electrolytes is to small. So they get especially important at the end of a charging or discharging cycles, which can be seen in the experiments in Appendix A.2 and A.3. Since also the volume flow influences the concentration overpotentials in general a higher volume flow is necessary for these operating points.
One common way to describe the concentration overpotentials is to express them in terms of Nernst's equation in combination with Fick's law of diffusion [14]. In the following steps, the overpotential caused by the limitation of MHQS for a charging cycle ($I_{\text{charge}} > 0$) is derived. The derivations for the other species can be done similarly. The concentration overpotential $\eta_{\text{MHQS,con}}$ is a consequence of the consumption of a MHQS at the electrode surface leading to a positive charging current. It is described with the concentrations of MHQS at the electrode surface $c_{\text{MHQS,surf}}$ and in the bulk electrolyte solution in the stack $c_{\text{MHQS,cell}}$, which is our state variable:

$$\eta_{\text{MHQS,con}} = \frac{RT}{zF} \ln \frac{c_{\text{MHQS,cell}}}{c_{\text{MHQS,surf}}} \tag{4.43}$$

To describe the difference between bulk and surface concentration, Fick's first law for one dimension can be used, which states that the molar flux J is proportional to the negative concentration gradient times a diffusivity constant D:

$$J = -D \frac{dc}{dx} \tag{4.44}$$

The spatial derivative of the concentrations can be approximated with

$$-\frac{dc}{dx} \approx \frac{c_{\text{MHQS,cell}} - c_{\text{MHQS,surf}}}{\delta} \tag{4.45}$$

, where δ is the thickness of the diffusion layer. By introduction of the local mass transfer coefficient $k_{m,MHQS} = \frac{D}{\delta}$ and linking the molar flux to the applied current towards an equivalent plate electrode with area A_{e} one gets:

$$\frac{I_{\text{charge}}}{zFA_{\text{e}}} = k_{m,MHQS} \left(c_{\text{MHQS,cell}} - c_{\text{MHQS,surf}} \right) \tag{4.46}$$

Note that by only using the effective electrode area A_{e} the local mass transfer coefficient implicitly also contains the ratio between real surface area of the carbon felt electrode and

the effective electrode area A_e. By combination of equation (4.43) and (4.46) the following expression is obtained:

$$\eta_{\text{MHQS,con}} = \left| \frac{RT}{zF} \ln\left(1 - \frac{I_{\text{charge}}}{zFA_e\, k_{\text{m,MHQS}}\, c_{\text{MHQS,cell}}}\right)\right| \quad , I_{\text{charge}} > 0 \tag{4.47}$$

If the same derivation is also done for the other species, the concentration overpotentials are computed by:

$$\eta_{\text{con}} = \begin{cases} \left|\frac{RT}{zF} \ln\left(1 - \frac{I_{\text{charge}}}{zFA_e\, k_{\text{m,MHQS}}\, c_{\text{MHQS,cell}}}\right)\right| + \left|\frac{RT}{zF} \ln\left(1 - \frac{I_{\text{charge}}}{zFA_e\, k_{\text{m,AQDS}}\, c_{\text{AQDS,cell}}}\right)\right| , I_{\text{charge}} > 0 \\ -\left|\frac{RT}{zF} \ln\left(1 - \frac{|I_{\text{charge}}|}{zFA_e\, k_{\text{m,MQS}}\, c_{\text{MQS,cell}}}\right)\right| - \left|\frac{RT}{zF} \ln\left(1 - \frac{|I_{\text{charge}}|}{zFA_e\, k_{\text{m,AHQDS}}\, c_{\text{AHQDS,cell}}}\right)\right| , I_{\text{charge}} \leq 0 \end{cases} \tag{4.48}$$

The local mass transfer coefficients k_m are dependent on the velocity the electrolyte is pumped through the electrode. The studies [15, 16] suggest an expression like

$$k_m = \kappa v^{0.4} \tag{4.49}$$

for dependence on the velocity, where κ is a parameter to be determined. By substitution of $v = \frac{\dot{V}}{A_{\text{flow}}}$ and definition of a new parameter $\bar{\kappa} = \frac{\kappa}{A_{\text{flow}}^{0.4}}$, where A_{flow} is the cross-sectional area of the flow through the electrodes in the stack, one gets

$$k_m = \bar{\kappa} \dot{V}^{0.4} \tag{4.50}$$

as the dependency between the measured volume flow and the mass transfer coefficients. By combining equation (4.48) with (4.50) and substituting in our state variables (4.52) one gets

$$\eta_{\text{con}} = \begin{cases} \left|\frac{RT}{zF} \ln\left(1 - \frac{I_{\text{charge}}}{zFA_e\, \bar{\kappa}_{\text{MHQS}}\, \dot{V}_+^{0.4} x_2}\right)\right| + \left|\frac{RT}{zF} \ln\left(1 - \frac{I_{\text{charge}}}{zFA_e\, \bar{\kappa}_{\text{AQDS}}\, \dot{V}_-^{0.4} x_4}\right)\right| , I_{\text{charge}} > 0 \\ -\left|\frac{RT}{zF} \ln\left(1 - \frac{|I_{\text{charge}}|}{zFA_e\, \bar{\kappa}_{\text{MQS}}\, \dot{V}_+^{0.4} x_1}\right)\right| - \left|\frac{RT}{zF} \ln\left(1 - \frac{|I_{\text{charge}}|}{zFA_e\, \bar{\kappa}_{\text{AHQDS}}\, \dot{V}_-^{0.4} x_3}\right)\right| , I_{\text{charge}} \leq 0 \end{cases} \tag{4.51}$$

to calculate the total concentration overpotential.

4.1.5. Resulting electro-chemical model

This section summarizes all of the previous sections to give an overview of the electro-chemical model developed. Figure 4.5 shows the structure for the simulation of the electro-chemical model. Hereby the state vector $\mathbf{x}$ holding the concentrations is defined by:

$$\mathbf{x} = \begin{bmatrix} c_{\text{MQS,cell}} \\ c_{\text{MHQS,cell}} \\ c_{\text{AHQDS,cell}} \\ c_{\text{AQDS,cell}} \\ c_{\text{MQS,tank}} \\ c_{\text{MHQS,tank}} \\ c_{\text{AHQDS,tank}} \\ c_{\text{AQDS,tank}} \end{bmatrix} \tag{4.52}$$

The dynamics of these concentrations are modelled by the **Concentration model**, which is

$$\frac{d}{dt}\mathbf{x} = \begin{bmatrix} \frac{-\dot{V}_+}{V_{\text{stack}}} & 0 & 0 & 0 & \frac{\dot{V}_+}{V_{\text{stack}}} & 0 & 0 & 0 \\ 0 & \frac{-\dot{V}_+}{V_{\text{stack}}} & 0 & 0 & 0 & \frac{\dot{V}_+}{V_{\text{stack}}} & 0 & 0 \\ 0 & 0 & \frac{-\dot{V}_-}{V_{\text{stack}}} & 0 & 0 & 0 & \frac{\dot{V}_-}{V_{\text{stack}}} & 0 \\ 0 & 0 & 0 & \frac{-\dot{V}_-}{V_{\text{stack}}} & 0 & 0 & 0 & \frac{\dot{V}_-}{V_{\text{stack}}} \\ \frac{\dot{V}_+}{V_{\text{tank}}} & 0 & 0 & 0 & \frac{-\dot{V}_+}{V_{\text{tank}}} & 0 & 0 & 0 \\ 0 & \frac{\dot{V}_+}{V_{\text{tank}}} & 0 & 0 & 0 & \frac{-\dot{V}_+}{V_{\text{tank}}} & 0 & 0 \\ 0 & 0 & \frac{\dot{V}_-}{V_{\text{tank}}} & 0 & 0 & 0 & \frac{-\dot{V}_-}{V_{\text{tank}}} & 0 \\ 0 & 0 & 0 & \frac{\dot{V}_-}{V_{\text{tank}}} & 0 & 0 & 0 & \frac{-\dot{V}_-}{V_{\text{tank}}} \end{bmatrix} \mathbf{x} + \frac{N_{\text{cells}}}{zFV_{\text{stack}}} \begin{bmatrix} 1 \\ -1 \\ 1 \\ -1 \\ 0 \\ 0 \\ 0 \\ 0 \end{bmatrix} \left(I_{\text{charge}} - \frac{U_{\text{stack}}}{R_{\text{loss}}} \right) \tag{4.53}$$

The first two output equations of the system, delivering E_+ and E_-, are described by the **Redox potential model**, which consists of the two equations:

$$E_+ = E_{0+} + \frac{RT}{zF} \ln\left(\frac{x_5}{x_6}\right) \tag{4.54}$$

$$E_- = E_{0-} + \frac{RT}{zF} \ln\left(\frac{x_8}{x_7}\right) \tag{4.55}$$

The third output of the system the cell voltage U_{cell} is calculated by the sum:

$$U_{\text{cell}} = U_{\text{OCV}} + \eta_{\text{ohm}} + \eta_{\text{act}} + \eta_{\text{con}} \tag{4.56}$$

The multiplication of the cell voltage with the number of cells N_{cells}, which gives the stack voltage U_{stack}, is used as input for the concentration model.
The different terms adding up to the cell voltage are calculated by their own model. The first term, the Open-Circuit-Voltage U_{OCV}, is calculated by the **OCV model**, which is described by the equation:

$$U_{\text{OCV}} = k_{\text{OCV}} \left[E_{0+} - E_{0-} + \frac{RT}{zF} \ln\left(\frac{x_1 x_3}{x_2 x_4}\right) \right] + d_{\text{OCV}} \tag{4.57}$$

The **ohmic overpotential model** calculates ohmic overpotential η_{ohm} by:

$$\eta_{\text{ohm}} = \begin{cases} R_{\text{charge}} \cdot I_{\text{charge}} & \text{for } I_{\text{charge}} \geq 0 \\ R_{\text{discharge}} \cdot I_{\text{charge}} & \text{for } I_{\text{charge}} < 0 \end{cases} \tag{4.58}$$

The **activation overpotential model** calculates the total activation overpotential η_{act} by:

$$\eta_{\text{act}} = \eta_{\text{act,+}} - \eta_{\text{act,-}} \tag{4.59}$$

$$\eta_{\text{act,+}} = \begin{cases} \frac{RT}{(1-\alpha_+)zF} \sinh^{-1}\left(\frac{I_{\text{charge}}}{2I_{0,+}}\right) & I_{\text{charge}} \geq 0 \\ \frac{RT}{\alpha_+ zF} \sinh^{-1}\left(\frac{I_{\text{charge}}}{2I_{0,+}}\right) & I_{\text{charge}} < 0 \end{cases} \tag{4.60}$$

$$I_{0,+} = zFA_{\text{e}}\, k_{0,+}\, c_{MQS,\text{cell}}^{1-\alpha_+}\, c_{\text{MHQS,cell}}^{\alpha_+} = zFA_{\text{e}}\, k_{0,+}\, x_1^{1-\alpha_+}\, x_2^{\alpha_+} \tag{4.61}$$

$$\eta_{\text{act,-}} = \begin{cases} \frac{RT}{(1-\alpha_-)zF} \sinh^{-1}\left(\frac{-I_{\text{charge}}}{2I_{0,-}}\right) & I_{\text{charge}} < 0 \\ \frac{RT}{\alpha_- zF} \sinh^{-1}\left(\frac{-I_{\text{charge}}}{2I_{0,-}}\right) & I_{\text{charge}} \geq 0 \end{cases} \tag{4.62}$$

$$I_{0,-} = zFA_{\text{e}}\, k_{0,-}\, c_{\text{AQDS,cell}}^{1-\alpha_-}\, c_{\text{AHQDS,cell}}^{\alpha_-} = zFA_{\text{e}}\, k_{0,-}\, x_4^{1-\alpha_-} x_3^{\alpha_-} \tag{4.63}$$

The **concentration overpotential model** calculates the concentration overpotential η_{con} by:

$$\eta_{\text{con}} = \begin{cases} \left|\frac{RT}{zF}\ln\left(1-\frac{I_{\text{charge}}}{zFA_{\text{e}}\,\bar{\kappa}_{\text{MHQS}}\,\dot{V}_{+}^{0.4}x_2}\right)\right| + \left|\frac{RT}{zF}\ln\left(1-\frac{I_{\text{charge}}}{zFA_{\text{e}}\,\bar{\kappa}_{\text{AQDS}}\,\dot{V}_{-}^{0.4}x_4}\right)\right|, I_{\text{charge}} > 0 \\ -\left|\frac{RT}{zF}\ln\left(1-\frac{|I_{\text{charge}}|}{zFA_{\text{e}}\,\bar{\kappa}_{\text{MQS}}\,\dot{V}_{+}^{0.4}x_1}\right)\right| - \left|\frac{RT}{zF}\ln\left(1-\frac{|I_{\text{charge}}|}{zFA_{\text{e}}\,\bar{\kappa}_{\text{AHQDS}}\,\dot{V}_{-}^{0.4}x_3}\right)\right|, I_{\text{charge}} \leq 0 \end{cases} \tag{4.64}$$

Since many of the model parameters are not known, section 4.2 will focus on the parametrization of the whole model.

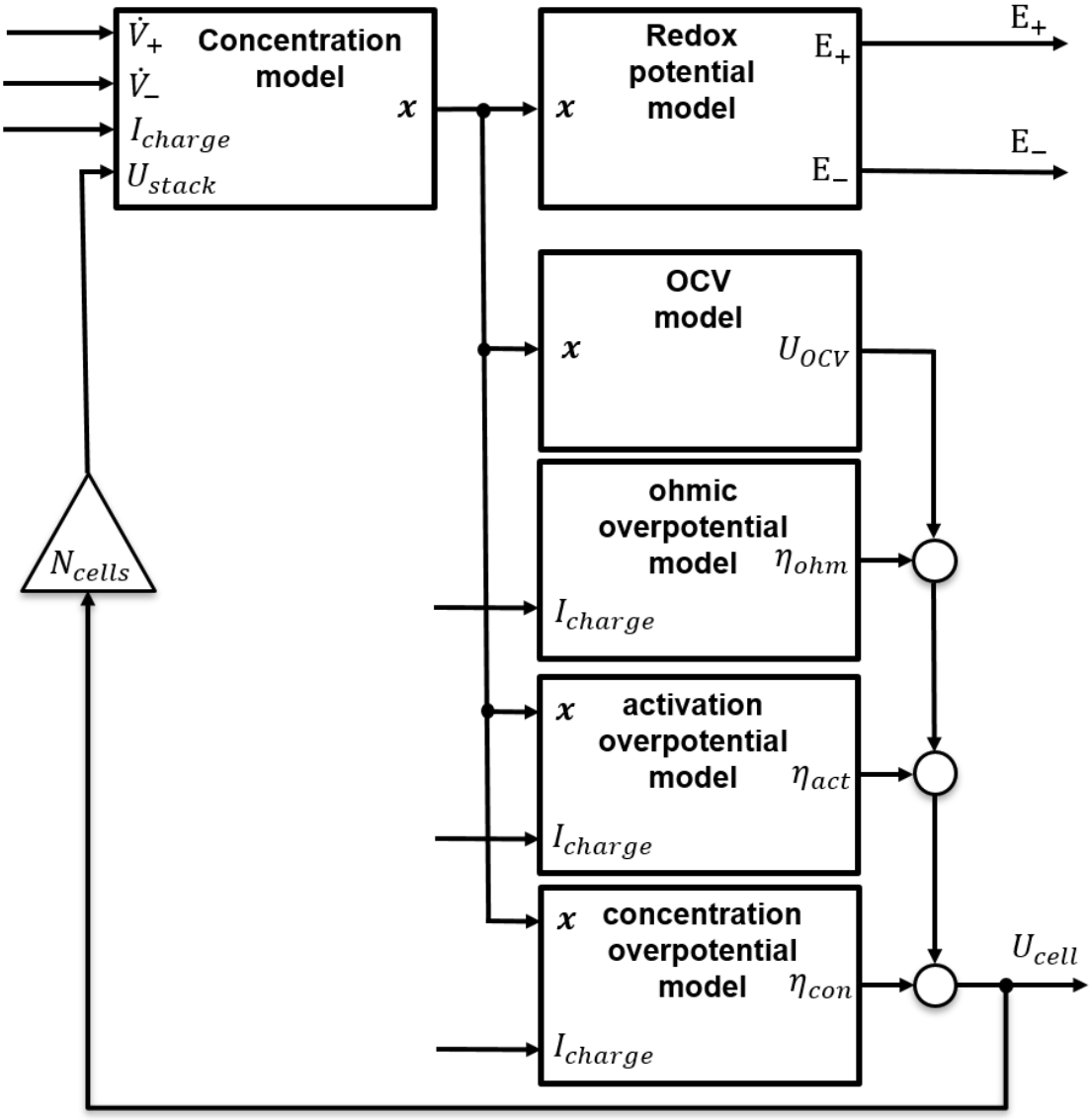

Figure 4.5.: Structure of the simulation of the electro-chemical model.

4.2. Model parameter determination

Quite a lot of the parameters of the model derived in section 4.1 are not known and have to be determined by a parameter optimization. Parameters to be determined are:

- The equivalent resistance accounting for the shunt current losses R_{loss}
- The electrode porosity ϵ_{por}
- The two formal potentials at the redox probes E_{0+} and E_{0-}
- The resistances for the ohmic overpotential R_{charge} and $R_{\text{discharge}}$
- The charge transfer coefficients for the activation overpotentials α_+ and α_-
- The standard rate constants $k_{0,+}$ and $k_{0,-}$
- The 4 parameters for the concentration overpotentials $\bar{\kappa}_{\text{MHQS}}$, $\bar{\kappa}_{\text{MQS}}$, $\bar{\kappa}_{\text{AQDS}}$ and $\bar{\kappa}_{\text{AHQDS}}$

All together this makes 14 model parameters to determine. Additionally also the initial concentrations for the experiments used for the parameter estimation are unknown, which would increase the total number of unknowns by 8 variables. But by choosing measurement data, such that the charging current has been zero for a sufficient amount of time, here 2 minutes, the assumption can be made that the cell and tank concentrations are the same. This reduces the number of additional variables to only 4. So the total number of unknown is 18.
To determine this unknown model parameters and the initial conditions a two step optimization problem is formulated in section 4.2.1 and solved with an algorithm called particle swarm optimization PSO, which is explained briefly in section 4.2.2. The results are shown in section 4.2.3.

4.2.1. Formulation of the parameter estimation problem

The number of unknowns is quite high, leading towards an estimation problem difficult to solve. Therefore, the parameter optimization problem is split into two separate problems. This is possible because our system has multiple outputs, where the different model parameters only or mainly influence one of the outputs. The first problem only uses the redox probes as outputs of the system. This enables to determine the initial concentrations and the relevant model parameters R_{loss}, E_{0+} and E_{0-} (see section 4.2.1.1). The second problem, see section 4.2.1.2, takes the already determined parameters and the initial concentrations and determines the missing parameters, which all are linked to the cell voltage. Here the cell voltage is used in the cost function. Note that for the second optimization problem the same experiment as for the first one has to be used, because the initial concentrations are now known for this experiment. The experiment used here can be seen in Appendix A.3.

4.2.1.1. Parameter estimation using the redox probes measurements

The first optimization problem uses the **Concentration model** the **Redox potential model** to simulate for the needed model parameters and initial conditions the redox potentials at

the redox probes. The structure of this reduced simulation can be seen in Figure 4.6, with the **concentration model** using the measured signals $\dot{V}_+$, $\dot{V}_-$, I_{charge} and U_{stack} as input signals, to compute the concentrations **x**. Note that for simulation of the concentration model the electrode porosity ϵ_{por} is needed, but it is not included in the parameter vector. Instead it is set to 0.9, which should be close to its real value according to literature. The influence of ϵ_{por} is small for the redox probes compared to the influence on the cell voltage. Therefore the electrode porosity ϵ_{por} will be determined by the second optimization problem instead. Based on the concentrations **x** the **redox potential model** calculates the corresponding redox potentials. Since also the initial concentrations are not

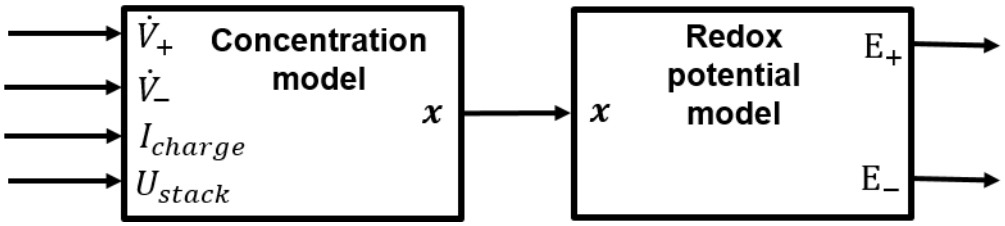

Figure 4.6.: Depiction of the simulation of the redox potentials.

known they have to be estimated as well. Instead of using the initial concentrations it is advantageous to use the initial State-of-Charge for both electrolytes $SOC_+(t=0)$ and $SOC_-(t=0)$ and the maximal concentrations in the electrolytes $c_{+,\max}$ and $c_{-,\max}$ instead. It is easier to find reasonable boundaries for these variables, which are needed for the particle swarm optimization. The State-of-Charge has to be between 0 and 1, and the maximal concentrations can't exceed the theoretical value known from the filling process. The initial concentrations can be easily computed by:

$$c_{\text{MQS}}(t=0) = c_{+,\max} SOC_+(t=0) \tag{4.65}$$
$$c_{\text{MHQS}}(t=0) = c_{+,\max}\,(1 - SOC_+(t=0)) \tag{4.66}$$
$$c_{\text{AHQDS}}(t=0) = c_{-,\max} SOC_-(t=0) \tag{4.67}$$
$$c_{\text{AQDS}}(t=0) = c_{-,\max}\,(1 - SOC_-(t=0)) \tag{4.68}$$

The parameters to be determined are stored in the parameter vector $\mathbf{x}_{\text{par1}}$:

$$\mathbf{x}_{\text{par1}} = \begin{bmatrix} c_{+,\max} \\ c_{-,\max} \\ SOC_+(t=0) \\ SOC_-(t=0) \\ E_{0+} \\ E_{0-} \\ R_{\text{loss}} \end{bmatrix} \tag{4.69}$$

The boundaries for the formal potentials E_{0+} and E_{0-} can be defined by the maximum and minimum value of the measured signal. The boundaries for R_{loss} are not that easy to set, some trial and error is the easiest approach here.
The difference between the simulated redox potentials and the measured one can be used to formulate the cost function of the optimization problem. Here the mean squared error

will be used as cost function $J_1((\mathbf{x}_{par1}))$ here:

$$J_1(\mathbf{x}_{\text{par1}}) = \sqrt{\frac{1}{2N}\sum_{j=1}^{N}\left[\left(E_{+,\text{sim},j} - E_{+,\text{meas},j}\right)^2 + \left(E_{\text{-},\text{sim},j} - E_{\text{-},\text{meas},j}\right)^2\right]} \tag{4.70}$$

Hereby N is the number of data points, and $E_{+,\text{sim},j}$, $E_{+,\text{meas},j}$, $E_{\text{-},\text{sim},j}$ and $E_{\text{-},\text{meas},j}$ are the simulated and measured redox potentials at the data point j respectively.

4.2.1.2. Parameter estimation using the measurement of the cell voltage

To determine the remaining parameters, the second optimization problem uses the cell voltage U_{cell}, which can be calculated from measured stack voltage U_{stack} by dividing it by the number of cells N_{cells}. Almost all of the remaining unknown parameters only influence the calculation of the cell voltage. The only exception is ϵ_{por}, which has a minor influence on the redox probes as well, but the influence on the cell voltage is much bigger. The parameter vector is:

$$\mathbf{x}_{\text{par2}} = \begin{bmatrix} \epsilon_{\text{por}} \\ R_{\text{charge}} \\ R_{\text{discharge}} \\ k_{0,+} \\ \alpha_{+} \\ k_{0,\text{-}} \\ \alpha_{\text{-}} \\ \bar{\kappa}_{\text{MQS}} \\ \bar{\kappa}_{\text{MHQS}} \\ \bar{\kappa}_{\text{AHQDS}} \\ \bar{\kappa}_{\text{AQDS}} \end{bmatrix} \tag{4.71}$$

The particle swarm optimization needs predefined boundaries for the optimization problem. For the parameter ϵ_{por} the boundaries can be set at 0.5 and 1 respectively. The boundaries for the other parameters are difficult to set without any previous knowledge. One option is to set the upper and lower boundaries quite far apart, some orders of magnitude, and start the optimization process with a very limited amount of iterations. If the final values of the parameters, derived by this limited optimization process, is a good indicator in which range the optimal parameter values might lie. If a parameter is close to a boundary it has to be extended. If the parameter is far from every boundary the boundaries can be made tighter. Tight boundaries decrease the time for the optimization a lot.
For a given parameter vector the cell voltage can be simulated. Figure 4.7 shows the principle structure of the simulation. The **concentration model** is calculating the concentrations stored in the state vector $\mathbf{x}$. Based on the concentrations the **OCV model** calculates U_{OCV}. The **ohmic overpotential model** calculates the ohmic overpotential η_{ohm} from the charging current I_{charge}. The **activation overpotential model** calculates η_{act} from I_{charge} and $\mathbf{x}$. The **concentration overpotential model** calculates η_{con} from I_{charge} and $\mathbf{x}$. By adding up U_{OCV} and all overpotentials one gets the cell voltage U_{cell}.

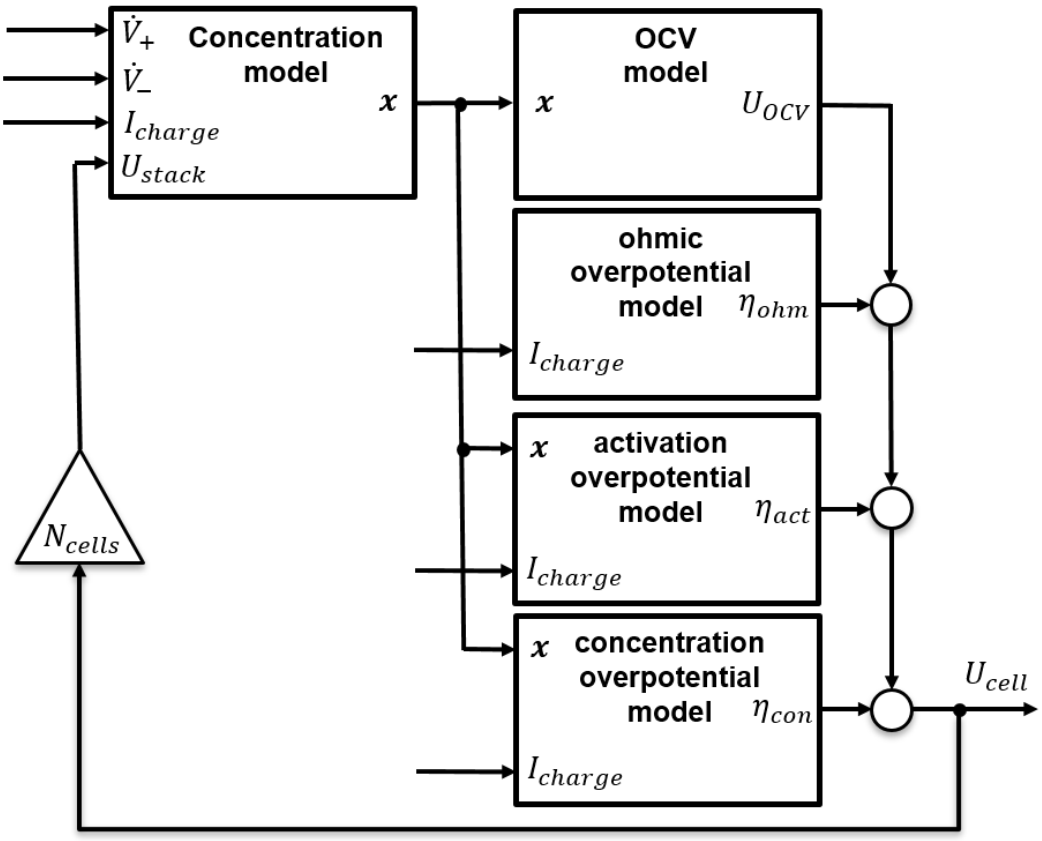

Figure 4.7.: Depiction of the simulation of the cell voltage.

The costfunction $J_2(\mathbf{x}_{\text{par2}})$ for the optimization problem consists of a combination of the mean square error and the maximum absolute error of the simulated cell voltage $U_{\text{cell,sim},j}$ and the measured cell voltage $U_{\text{cell,meas},j}$ for the j-th data point.

$$J_2(\mathbf{x}_{\text{par2}}) = \sqrt{\frac{1}{N}\sum_{j=1}^{N}\left(U_{\text{cell,sim},j} - U_{\text{cell,meas},j}\right)^2} + c_{\text{w}} \max_{j\in[1,N]} \left|U_{\text{cell,sim},j} - U_{\text{cell,meas},j}\right| \quad (4.72)$$

Here N is the total number of data points used and c_{w}, here chosen to be 0.5, is a weighting factor to balance the influence of the different terms. The term with the maximum absolute error showed to be helpful for the convergence of the optimization problem.

4.2.2. Particle Swarm Optimization

The described optimization problems in section 4.2.1 are not easy to optimize, because of the high number of unknowns, the fact that the system is able to diverge in finite time due to the non-linear output equations and multiple local optima deterministic optimization algorithms are not suitable. Therefore Particle Swarm Optimization PSO was used, because it is a quite simple meta-heuristic algorithm, which is able to overcome local optima. This section briefly describes the working principle of Particle Swarm Optimization PSO. PSO is an optimization algorithm imitating the behaviour of a swarm to find the optimum. Here

the swarm consists of several particles, which are initialized with a random position in the solution space of the optimization problem. Additionally each particle gets a velocity to travel through the solution space, which is also initialized randomly. Now, the following steps are all executed iteratively. Based on the position of the particles their costs are computed by the costfunction. The position and the cost of the particle with the best costs gets stored. Then the velocity and position of the particles gets updated. The velocity of the i-th particle is updated by:

$$v_i^{n+1} = wv_i^n + c_1 r_1 \left(p_{\text{best},i}^n - p_i^n \right) + c_2 r_2 \left(p_{\text{best,global}}^n - p_i^n \right) \tag{4.73}$$

Here v_i^{n+1} is the velocity for the next iteration, where n is the number of the current iteration. The part wv_i^n is called inertia, because it uses the velocity of the current iteration v_i^n multiplied by the inertia coefficient w, which is decreased each iteration, by multiplying it with a damping factor. The inertia term helps in overcoming local optima. The part $c_1 r_1 \left(p_{\text{best},i}^n - p_i^n \right)$ represents an velocity component in the direction of the position, where the particle experienced the best costs until now $p_{\text{best},i}$. Here p_i^n is the current position of the particle, c_1 is called the personal acceleration coefficient and r_1 is a random number. The part $c_2 r_2 \left(p_{\text{best,global}}^n - p_i^n \right)$ introduces the influence of the other particles and is responsible for the swarm behaviour. It is a velocity component in the direction of the global best position $p_{\text{best,global}}^n$ yet. c_2 is called social acceleration coefficient and r_2 is again a random number. The new position p_i^{n+1} is computed by:

$$p_i^{n+1} = p_i^n + v_i^{n+1} \tag{4.74}$$

Then again the costs are calculated and the personal and global bests are determined. This repeats until a termination condition is fulfilled or the maximal number of iterations is reached. Note that it isn't guaranteed, that the solution found might be stuck in a local minima. So restarting the optimization process again might give a different result and should be done to check the result.
Figure 4.8 depicts the update of velocity and position of one particle. The green arrows hereby symbolise the different velocity components, which add up to the new velocity.

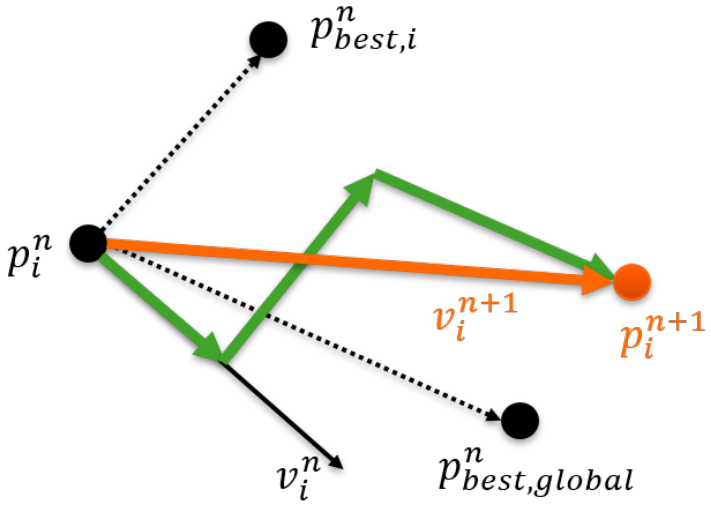

Figure 4.8.: Update of velocity and position of one particle.

4.2.3. Results of the parameter estimation

By solving the optimization problems described in section 4.2.1.1 and section 4.2.1.2 with Particle Swarm Optimization the solution from Table 4.1 for the model parameters is obtained.

parameter	unit	value
E_{0+}	V	0.3373
E_{0-}	V	-0.0470
R_{loss}	Ω	513.6
ϵ_{por}	-	0.9242
R_{charge}	Ω	0.0017
$R_{\text{discharge}}$	Ω	0.0503
$k_{0,+}$	$\frac{m}{s}$	1.136e-05
α_+	-	0.8344
$k_{0,-}$	$\frac{m}{s}$	4.198e-06
α_-	-	0.3725
$\bar{\kappa}_{\text{MQS}}$	$\left(\frac{s^2}{m}\right)^{0.2}$	0.0203
$\bar{\kappa}_{\text{MHQS}}$	$\left(\frac{s^2}{m}\right)^{0.2}$	1.6213
$\bar{\kappa}_{\text{AHQDS}}$	$\left(\frac{s^2}{m}\right)^{0.2}$	0.5769
$\bar{\kappa}_{\text{AQDS}}$	$\left(\frac{s^2}{m}\right)^{0.2}$	1.5782

Table 4.1.: Determined model parameters.

The comparison of the measurements of the experiment from Appendix A.3 with simulation of the whole model from section 4.1.5 with the determined parameter set and initial conditions leads to the result shown in Figure 4.9. Here the uppermost plot shows

the measured charging current of the chosen experiment, which is used as input to the simulation. The second plot shows the corresponding measured and simulated redox potentials. It can be seen that the model is able to capture the behaviour of the negative redox potential E_- quite well. For the positive redox potential E_+ the simulated model deviates noticeable from the measurement for a high or low State-of-Charge. Especially at the end of the charge processes the model error is high. Obviously the model is not able to capture all characteristics of the positive electrolyte. The third plot shows the cell voltage U_{cell}. The simulation and measurement of the cell voltage hereby have a quite good agreement. Only at the end of charge and discharge cycles the model deviates from the measurement significantly. One reason for these deviations is probably the fact, that for low concentrations of one of the reactants the activity is much lower than 1, which was implicitly assumed by the used version of Nernst's equation in this thesis.

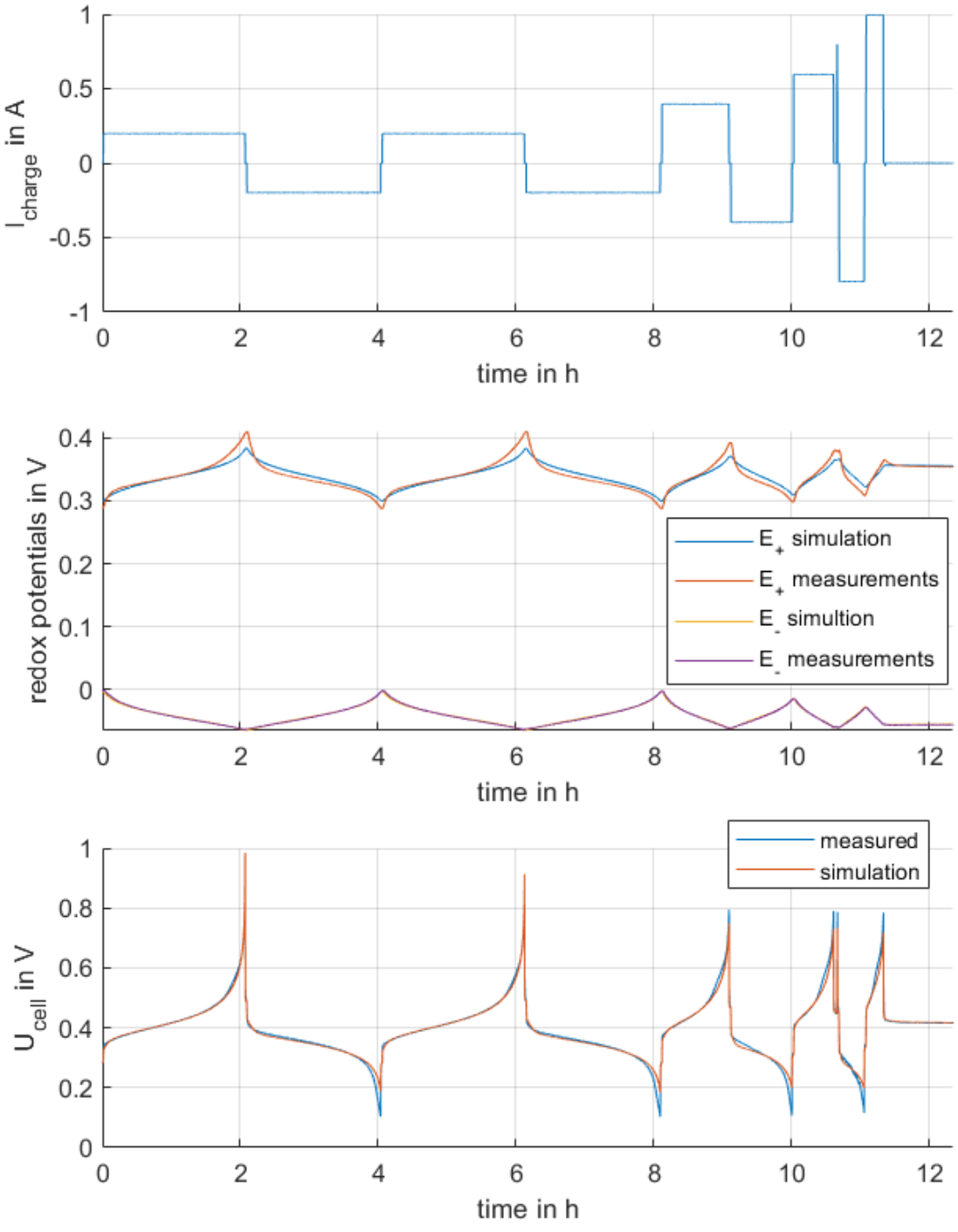

Figure 4.9.: Results of the model parameter estimation.

4.3. Online State-of-Charge estimation

The final goal of this chapter is to find a method for estimating the State-of-Charge SOC online. Therefore a simple method using an inversion of Nernst's equation is presented in section 4.3.1. A more advanced method using an observer from literature is presented in section 4.3.2.

4.3.1. Inversion of Nernst's Equation for State-of-Charge estimation

A simple approach for estimating the SOCs of both electrolytes uses the redox potential measurements. Starting from Nernst's Equation for the positive-side electrolyte in equation (4.27) and inserting $c_{\mathrm{MQS,tank}} = SOC_{+}c_{+,\max}$ and $c_{\mathrm{MHQS,tank}} = (1 - SOC_{+})c_{+,\max}$, where $c_{+,\max}$ is the maximum concentration and SOC_{+}) is the State-of-charge for the positive-side electrolyte, one gets:

$$E_{+} = E_{0+} + \frac{RT}{zF} \ln\left(\frac{SOC_{+}c_{+,\max}}{(1 - SOC_{+})c_{+,\max}}\right) \tag{4.75}$$

By cancelling $c_{+,\max}$ and solving for the positive side electrolyte SOC_{+} gets:

$$SOC_{+} = \frac{e^{\frac{E_{+} - E_{0+}}{\frac{RT}{zF}}}}{1 + e^{\frac{E_{+} - E_{0+}}{\frac{RT}{zF}}}} \tag{4.76}$$

So SOC_{+} can be directly determined from the measurement of the positive-side redox potential. Notice that this approach implicitly assumes that the concentrations in tank and stack are the same, which leads to an small error only if the tank volume is much bigger than the stack volume.
The same can also be done for the negative-side electrolyte. Rearranging equation (4.26) similarly leads to:

$$SOC_{-} = \frac{1}{1 + e^{\frac{E_{-} - E_{0-}}{\frac{RT}{zF}}}} \tag{4.77}$$

Figure 4.10 shows the results of the approach presented in this section. The first plot shows the charging current applied in this experiment. The second plot shows the estimated States-of-Charge in % for the positive electrolyte SOC_{+} and the negative electrolyte SOC_{-}. For a constant charging current the SOCs should increase and decrease with a constant slope, which is the case for SOC_{-}, but not for SOC_{+}. This can be definitively traced back to the deviations from the model. The big disadvantage of this method is that only the two SOCs can be determined, but it is not possible to determine the maximal storable charge of both sides $Q_{\max,+}$ and $Q_{\max,-}$. Therefore a more advanced approach will be discussed in the next section.

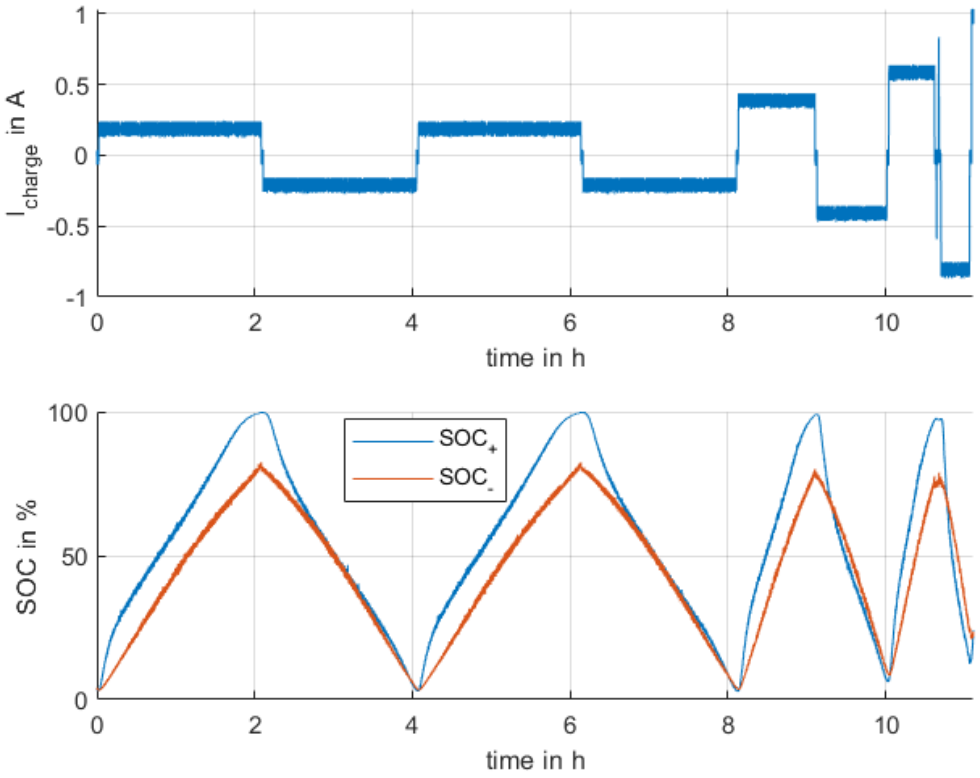

Figure 4.10.: Result of the SOC estimation with the inverted Nernst equation.

4.3.2. State-of-Charge observer

To estimate not only the SOCs, but also the maximal storable charge, a state observer will be designed following an approach based on a paper for vanadium flow batteries [17] to estimate the concentrations. The step by step derivation of this observer from the developed model is shown in section 4.3.2.1. The validation of this observer can be seen in section 4.3.2.2.

4.3.2.1. Formulation of the State-of-Charge observer

Following the approach of [17] an observer for the developed system is presented in this section. The main steps here are the development of a trivial observer for the stable parts of the dynamics, the outputs of this trivial observer then are used as input of a non-linear observer. To use this non-linear observer the remaining system has to be brought in a specific form.
The first step for the observer design is separation of the dynamics of the concentration

difference between stack and tank.

$$\Delta c_{\mathrm{MQS}} = c_{\mathrm{MQS,stack}} - c_{\mathrm{MQS,tank}} \tag{4.78}$$
$$\Delta c_{\mathrm{MHQS}} = c_{\mathrm{MHQS,stack}} - c_{\mathrm{MHQS,tank}} \tag{4.79}$$
$$\Delta c_{\mathrm{AHQDS}} = c_{\mathrm{AHQDS,stack}} - c_{\mathrm{AHQDS,tank}} \tag{4.80}$$
$$\Delta c_{\mathrm{AQDS}} = c_{\mathrm{AQDS,stack}} - c_{\mathrm{AQDS,tank}} \tag{4.81}$$

The corresponding dynamics are:

$$\frac{d}{dt}\Delta c_{\mathrm{MQS}} = -\dot{V}_{+}\left(\frac{1}{V_{\mathrm{stack}}} + \frac{1}{V_{\mathrm{tank}}}\right)\Delta c_{\mathrm{MQS}} + \frac{N_{\mathrm{cells}}}{zFV_{\mathrm{stack}}}\left(I_{\mathrm{charge}} - \frac{U_{\mathrm{stack}}}{R_{\mathrm{loss}}}\right) \tag{4.82}$$
$$\frac{d}{dt}\Delta c_{\mathrm{MHQS}} = -\dot{V}_{+}\left(\frac{1}{V_{\mathrm{stack}}} + \frac{1}{V_{\mathrm{tank}}}\right)\Delta c_{\mathrm{MHQS}} - \frac{N_{\mathrm{cells}}}{zFV_{\mathrm{stack}}}\left(I_{\mathrm{charge}} - \frac{U_{\mathrm{stack}}}{R_{\mathrm{loss}}}\right) \tag{4.83}$$
$$\frac{d}{dt}\Delta c_{\mathrm{AHQDS}} = -\dot{V}_{-}\left(\frac{1}{V_{\mathrm{stack}}} + \frac{1}{V_{\mathrm{tank}}}\right)\Delta c_{\mathrm{AHQDS}} + \frac{N_{\mathrm{cells}}}{zFV_{\mathrm{stack}}}\left(I_{\mathrm{charge}} - \frac{U_{\mathrm{stack}}}{R_{\mathrm{loss}}}\right) \tag{4.84}$$
$$\frac{d}{dt}\Delta c_{\mathrm{AQDS}} = -\dot{V}_{-}\left(\frac{1}{V_{\mathrm{stack}}} + \frac{1}{V_{\mathrm{tank}}}\right)\Delta c_{\mathrm{AQDS}} - \frac{N_{\mathrm{cells}}}{zFV_{\mathrm{stack}}}\left(I_{\mathrm{charge}} - \frac{U_{\mathrm{stack}}}{R_{\mathrm{loss}}}\right) \tag{4.85}$$

Note that these decoupled dynamics all have negative eigenvalues for the volume flows $\dot{V}_{+} > 0$ and $\dot{V}_{-} > 0$, which is the case for the battery in normal operation. So the concentration differences are asymptotically stable allowing to design a trivial observer with also stable error dynamics. A trivial observer is basically a copy of the plant dynamics. So the observer dynamics for the Δc-estimation looks like that:

$$\frac{d}{dt}\Delta \hat{c}_{\mathrm{MQS}} = -\dot{V}_{+}\left(\frac{1}{V_{\mathrm{stack}}} + \frac{1}{V_{\mathrm{tank}}}\right)\Delta \hat{c}_{\mathrm{MQS}} + \frac{N_{\mathrm{cells}}}{zFV_{\mathrm{stack}}}\left(I_{\mathrm{charge}} - \frac{U_{\mathrm{stack}}}{R_{\mathrm{loss}}}\right) \tag{4.86}$$
$$\frac{d}{dt}\Delta \hat{c}_{\mathrm{MHQS}} = -\dot{V}_{+}\left(\frac{1}{V_{\mathrm{stack}}} + \frac{1}{V_{\mathrm{tank}}}\right)\Delta \hat{c}_{\mathrm{MHQS}} - \frac{N_{\mathrm{cells}}}{zFV_{\mathrm{stack}}}\left(I_{\mathrm{charge}} - \frac{U_{\mathrm{stack}}}{R_{\mathrm{loss}}}\right) \tag{4.87}$$
$$\frac{d}{dt}\Delta \hat{c}_{\mathrm{AHQDS}} = -\dot{V}_{-}\left(\frac{1}{V_{\mathrm{stack}}} + \frac{1}{V_{\mathrm{tank}}}\right)\Delta \hat{c}_{\mathrm{AHQDS}} + \frac{N_{\mathrm{cells}}}{zFV_{\mathrm{stack}}}\left(I_{\mathrm{charge}} - \frac{U_{\mathrm{stack}}}{R_{\mathrm{loss}}}\right) \tag{4.88}$$
$$\frac{d}{dt}\Delta \hat{c}_{\mathrm{AQDS}} = -\dot{V}_{-}\left(\frac{1}{V_{\mathrm{stack}}} + \frac{1}{V_{\mathrm{tank}}}\right)\Delta \hat{c}_{\mathrm{AQDS}} - \frac{N_{\mathrm{cells}}}{zFV_{\mathrm{stack}}}\left(I_{\mathrm{charge}} - \frac{U_{\mathrm{stack}}}{R_{\mathrm{loss}}}\right) \tag{4.89}$$

Here $\Delta \hat{c}_i$ for $i \in \{\mathrm{MHQS, MQS, AQDS, AHQDS}\}$ are the estimates of the concentration differences. By choosing the initial conditions

$$\Delta \hat{c}_{\mathrm{MQS}}(0) = -\Delta \hat{c}_{\mathrm{MHQS}}(0) \tag{4.90}$$
$$\Delta \hat{c}_{\mathrm{AHQDS}}(0) = -\Delta \hat{c}_{\mathrm{AQDS}}(0) \tag{4.91}$$

the statements

$$\Delta \hat{c}_{\mathrm{MQS}}(t) = -\Delta \hat{c}_{\mathrm{MHQS}}(t), \forall t \geq 0 \tag{4.92}$$
$$\Delta \hat{c}_{\mathrm{AHQDS}}(t) = -\Delta \hat{c}_{\mathrm{AQDS}}(t), \forall t \geq 0 \tag{4.93}$$

hold, for proof see [17]. So for each electrolyte one state variable is sufficient and the concentration differences can be estimated by:

$$\frac{d}{dt}\Delta\hat{c}_{+} = -\dot{V}_{+}\left(\frac{1}{V_{\text{stack}}} + \frac{1}{V_{\text{tank}}}\right)\Delta\hat{c}_{+} + \frac{N_{\text{cells}}}{zFV_{\text{stack}}}\left(I_{\text{charge}} - \frac{U_{\text{stack}}}{R_{\text{loss}}}\right) \tag{4.94}$$

$$\Delta\hat{c}_{\text{MQS}} = \Delta\hat{c}_{+} \tag{4.95}$$

$$\Delta\hat{c}_{\text{MHQS}} = -\Delta\hat{c}_{+} \tag{4.96}$$

$$\frac{d}{dt}\Delta\hat{c}_{\text{-}} = -\dot{V}_{\text{-}}\left(\frac{1}{V_{\text{stack}}} + \frac{1}{V_{\text{tank}}}\right)\Delta\hat{c}_{\text{-}} + \frac{N_{\text{cells}}}{zFV_{\text{stack}}}\left(I_{\text{charge}} - \frac{U_{\text{stack}}}{R_{\text{loss}}}\right) \tag{4.97}$$

$$\Delta\hat{c}_{\text{AHQDS}} = \Delta\hat{c}_{\text{-}} \tag{4.98}$$

$$\Delta\hat{c}_{\text{AQDS}} = -\Delta\hat{c}_{\text{-}} \tag{4.99}$$

The remaining dynamics of the tank concentrations now can be expressed in terms of the concentration differences:

$$\frac{d}{dt}c_{\text{MQS,tank}} = \frac{\dot{V}_{+}}{V_{\text{tank}}}\Delta c_{+} \tag{4.100}$$

$$\frac{d}{dt}c_{\text{MHQS,tank}} = -\frac{\dot{V}_{+}}{V_{\text{tank}}}\Delta c_{+} \tag{4.101}$$

$$\frac{d}{dt}c_{\text{AHQDS,tank}} = \frac{\dot{V}_{\text{-}}}{V_{\text{tank}}}\Delta c_{\text{-}} \tag{4.102}$$

$$\frac{d}{dt}c_{\text{AQDS,tank}} = -\frac{\dot{V}_{\text{-}}}{V_{\text{tank}}}\Delta c_{\text{-}} \tag{4.103}$$

So the tank concentrations dynamics depend on Δc_{+} and $\Delta c_{\text{-}}$, which can be estimated by the equations (4.94) and (4.97) and can therefore be considered as known inputs. Following [17] new inputs are defined:

$$\mathbf{u} := \begin{bmatrix} u_{+} \\ u_{\text{-}} \end{bmatrix} := \begin{bmatrix} \frac{\dot{V}_{+}}{V_{\text{tank}}}\Delta c_{+} \\ \frac{\dot{V}_{\text{-}}}{V_{\text{tank}}}\Delta c_{\text{-}} \end{bmatrix} \tag{4.104}$$

Also the used outputs are redefined, such that the measured redox potentials are transformed according to the rearranged equations (4.27) and (4.26):

$$y_{+} := \frac{c_{\text{MQS,tank}}}{c_{\text{MHQS,tank}}} := \exp\left[\frac{zF}{RT}\left(E_{+} - E_{\text{o+}}\right)\right] \tag{4.105}$$

$$y_{-} := \frac{c_{\text{AQDS,tank}}}{c_{\text{AHQDS,tank}}} := \exp\left[\frac{zF}{RT}\left(E_{\text{-}} - E_{\text{o-}}\right)\right] \tag{4.106}$$

By defining the state vector for the tank concentrations

$$\mathbf{c}_{\text{tank}} := \begin{bmatrix} c_1 \\ c_2 \\ c_3 \\ c_4 \end{bmatrix} := \begin{bmatrix} c_{\text{MQS,tank}} \\ c_{\text{MHQS,tank}} \\ c_{\text{AHQDS,tank}} \\ c_{\text{AQDS,tank}} \end{bmatrix} \tag{4.107}$$

one gets the following system:

$$\begin{cases} \dot{\mathbf{c}}_{\text{tank}} = \begin{bmatrix} u_+ \\ -u_+ \\ u_- \\ -u_- \end{bmatrix} \\ y_+ = \frac{c_1}{c_2} \\ y_- = \frac{c_4}{c_3} \end{cases} \tag{4.108}$$

A state transformation according to [17] taking the concentration ratios and reciprocal maximal concentrations as state variables is used to transform the system into a more favourable form. The state transformation is:

$$\mathbf{z} := \Phi(\mathbf{c}_{\text{tank}}) = \begin{bmatrix} \frac{c_1}{c_2} \\ \frac{1}{c_1+c_2} \\ \frac{c_4}{c_3} \\ \frac{1}{c_3+c_4} \end{bmatrix} \tag{4.109}$$

With the inverse transformation:

$$\mathbf{c}_{\text{tank}} := \Phi^{-1}(\mathbf{z}) = \begin{bmatrix} \frac{z_1}{z_2(1+z_1)} \\ \frac{1}{z_2(1+z_1)} \\ \frac{1}{z_4(1+z_3)} \\ \frac{z_3}{z_4(1+z_3)} \end{bmatrix} \tag{4.110}$$

This leads to the transformed system:

$$\begin{cases} \dot{\mathbf{z}} = \begin{bmatrix} u_+ z_2(1+z_1)^2 \\ 0 \\ -u_- z_4(1+z_3)^2 \\ 0 \end{bmatrix} = \begin{bmatrix} \bar{u}_+ z_2(1+z_1)^2 \\ 0 \\ \bar{u}_- z_4(1+z_3)^2 \\ 0 \end{bmatrix} =: \mathbf{f}(\mathbf{z}, \bar{\mathbf{u}}) \\ y_+ = z_1 \\ y_- = z_3 \end{cases} \tag{4.111}$$

By the redefinition of $\bar{\mathbf{u}} := [\bar{u}_+ \quad \bar{u}_-]^\mathsf{T} := [u_+ \quad -u_-]^\mathsf{T}$ the system now has exactly the same form as in [17]. Therefore the proposed nonlinear observer can be used to estimate the states:

$$\dot{\hat{\mathbf{z}}} = \mathbf{f}(\hat{\mathbf{z}}, \bar{\mathbf{u}}) + \mathbf{g}(\hat{\mathbf{z}}, \mathbf{y}, \bar{\mathbf{u}}) + \mathbf{M}(\hat{\mathbf{z}}, \bar{\mathbf{u}}) \tag{4.112}$$

Here $\mathbf{f}(\hat{\mathbf{z}}, \bar{\mathbf{u}})$ is simply a copy of the systems dynamics in equation (4.111). $\mathbf{g}(\hat{\mathbf{z}}, \mathbf{y}, \bar{\mathbf{u}})$ is the correction term of the observer and $\mathbf{M}(\hat{\mathbf{z}})$ keeps the observers states inside predefined boundaries corresponding to physical constraints of the system. The correction term is:

$$\mathbf{g}(\hat{\mathbf{z}}, \mathbf{y}, \bar{\mathbf{u}}) = \begin{bmatrix} l\lambda_{1,+} [y_+ - \hat{z}_1] \\ l\lambda_{2,+} (\bar{u}_+) [y_+ - \hat{z}_1] \\ l\lambda_{1,-} [y_- - \hat{z}_3] \\ l\lambda_{2,-} (\bar{u}_-) [y_- - \hat{z}_3] \end{bmatrix}, \tag{4.113}$$

where the following conditions have to be fulfilled:

$$l \geq 1 \tag{4.114}$$
$$\lambda_{1,+} > 3\bar{u}_{\max}(1 + z_{1,\max})^2 \tag{4.115}$$
$$\lambda_{2,+}(\bar{u}_+) = \lambda_{1,+}\operatorname{sgn}(\bar{u}_+) \tag{4.116}$$
$$\lambda_{1,-} > 3\bar{u}_{\max}(1 + z_{3,\max})^2 \tag{4.117}$$
$$\lambda_{2,-}(\bar{u}_-) = \lambda_{1,-}\operatorname{sgn}(\bar{u}_-) \tag{4.118}$$

The variables $\bar{u}_{\max}$, $z_{1,\max}$ and $z_{3,\max}$ are upper bounds for $\bar{u}_\pm$, z_1 and z_3. $\bar{u}_{\max}$ can be calculated from the maximal possible current $I_{\max}$ by:

$$\bar{u}_{\max} = \frac{N_{\text{cells}}}{zF(V_{\text{stack}} + V_{\text{tank}})} I_{\max} \tag{4.119}$$

The term $\mathbf{M}(\hat{\mathbf{z}})$ is computed by:

$$\mathbf{M}(\hat{\mathbf{z}}, \bar{\mathbf{u}}) = -\gamma \mathbf{P}^{-1}(\bar{\mathbf{u}}) \frac{\partial \mathbf{r}(\hat{\mathbf{z}})}{\partial \mathbf{z}} \mathbf{r}(\hat{\mathbf{z}}) \tag{4.120}$$

Here the factor $\gamma > 0$ and $\mathbf{r}(\hat{\mathbf{z}})$ is a vector holding all $r_i = (\max\{z_{i,\min} - z_i; 0\})^2 + (\max\{z_i - z_{i,\max}; 0\})^2$ for $i = 1, 2, 3, 4$. The predefined boundaries $z_{i,\min}$ and $z_{i,\max}$ are set according to physical constraints of the system, where the concentration ratios typically lie between 0.01 and 100 and the boundaries for the reciprocal maximal concentration can be expressed in terms of the theoretical maximal concentration due to the knowledge from the filling process. $\mathbf{P}(\bar{\mathbf{u}})$ is the matrix

$$\mathbf{P}(\bar{\mathbf{u}}) = \begin{bmatrix} 8 & -\operatorname{sgn}(\bar{u}_+) & 0 & 0 \\ -\operatorname{sgn}(\bar{u}_+) & 1 & 0 & 0 \\ 0 & 0 & 8 & -\operatorname{sgn}(\bar{u}_-) \\ 0 & 0 & -\operatorname{sgn}(\bar{u}_-) & 1 \end{bmatrix} \tag{4.121}$$

which is used to show global asymptotic Lyapunov stability for the estimation error dynamics of the observer, see [17].
Putting all above together gets the observer structure, which can be seen in Figure 4.11. Here the Δc-estimation using equations (4.94)-(4.99) estimates the concentration differences. The transformed redox probe measurements y_+ and y_- are computed by the measurement transformation in equations (4.105) and (4.106). Using the transformed measurements and the estimated concentration difference the nonlinear observer (4.112) estimates the transformed state variables $\hat{\mathbf{z}}$. By applying the inverse state transformations (4.110) the estimate of the tank concentrations is obtained. The cell concentrations can be easily calculated by the equations (4.78)-(4.81). These estimates of cell and tank concentrations now can be used to calculate the SOC and maximal storable charge of both electrolytes using the definitions (4.4), (4.5), (4.6) and (4.7).

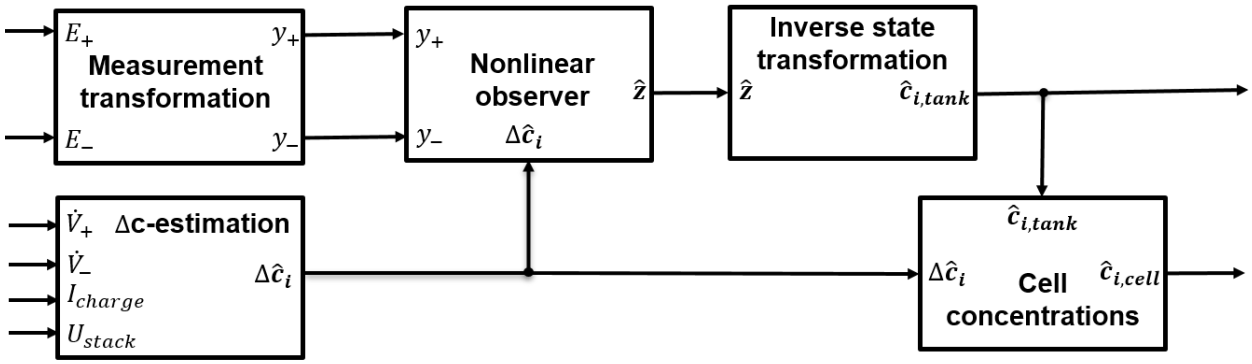

Figure 4.11.: Structure of the observer.

4.3.2.2. Experimental validation of the observer

The observer presented in section 4.3.2.1 is tested with measurement data. It appeared that the observer is very sensitive to measurement noise, due to its high gains. To reduce the effect of measurement noise the redox probe measurements are first applied to an lowpass filter. The results of the observer with the filtered measurements can be seen in Figure 4.12, where the uppermost plot shows the measured charging current I_{charge} of the used experiment. The second plot shows the estimated SOC_+ and SOC_- in %, they both behave in a very similar way to the simple approach, see section 4.3.1. The third plot shows the estimated maximal storable charge $Q_{\text{max,+}}$ and $Q_{\text{max,-}}$ in Ah. One can notice that the estimation for the negative-side electrolyte seems to work much better, than for the positive-side electrolyte. This obviously follows from the bigger model errors of the positive-side electrolytes. Especially the spikes in the estimate of $Q_{\text{max,+}}$ hints to the model errors at the end of charge cycles.
To check if the results of the observer are plausible the stored charge for both electrolytes $Q_\pm$ can be calculated by:

$$Q_+ = SOC_+ \cdot Q_{\text{max,+}} \tag{4.122}$$
$$Q_- = SOC_- \cdot Q_{\text{max,-}} \tag{4.123}$$

As comparison the stored charge can be computed via coulomb counting:

$$Q(t) = N_{\text{cells}} \int_0^t I_{\text{charge}}(\tau) d\tau \tag{4.124}$$

Here the assumption is made that the stored charge at the beginning is zero, which is approximately true after a finished discharge cycle. The data used for the plausibility check has therefore to be chosen accordingly. Figure 4.13 shows again the charging current in the upper plot and the corresponding signals Q_+, Q_- and Q for the stored charge in the bottom plot. We can see that it takes about 2 hours for Q_+ to converge. The reason probably is that due to the logarithm in the measurement transformation the observer isn't very sensitive for small values of the redox potential. This is a major setback of this observer design in my opinion. After the observer converged the three signal seem to be plausible estimates, except the spikes of Q_+. Note that this is only a plausibility check, the lines don't have to overlap, because the two electrolytes don't necessarily have the same

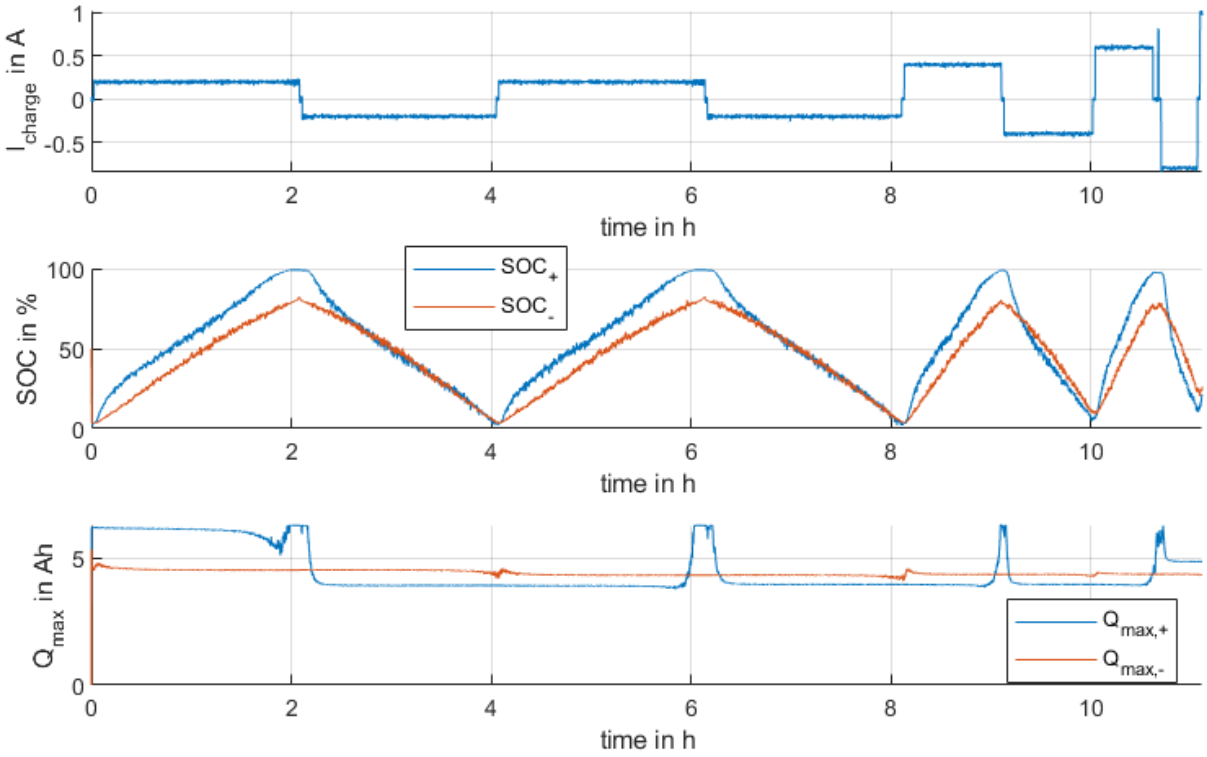

Figure 4.12.: Results of the observer estimation.

maximal capacity and might have asymmetric SOCs. Additionally the coulomb counting's initial condition might be of and it doesn't consider any losses. The spikes in Q_+ as already discussed are caused by model errors. To conclude, the observer is able to estimate the SOCs and maximal storable charge within the limitations due to the underlying model accuracy, but the high noise sensitivity and the convergence only at high redox potential values are serious downsides. Maybe an Kalman Filter based approach, instead of the non-linear observer in [17], could improve the estimations further.

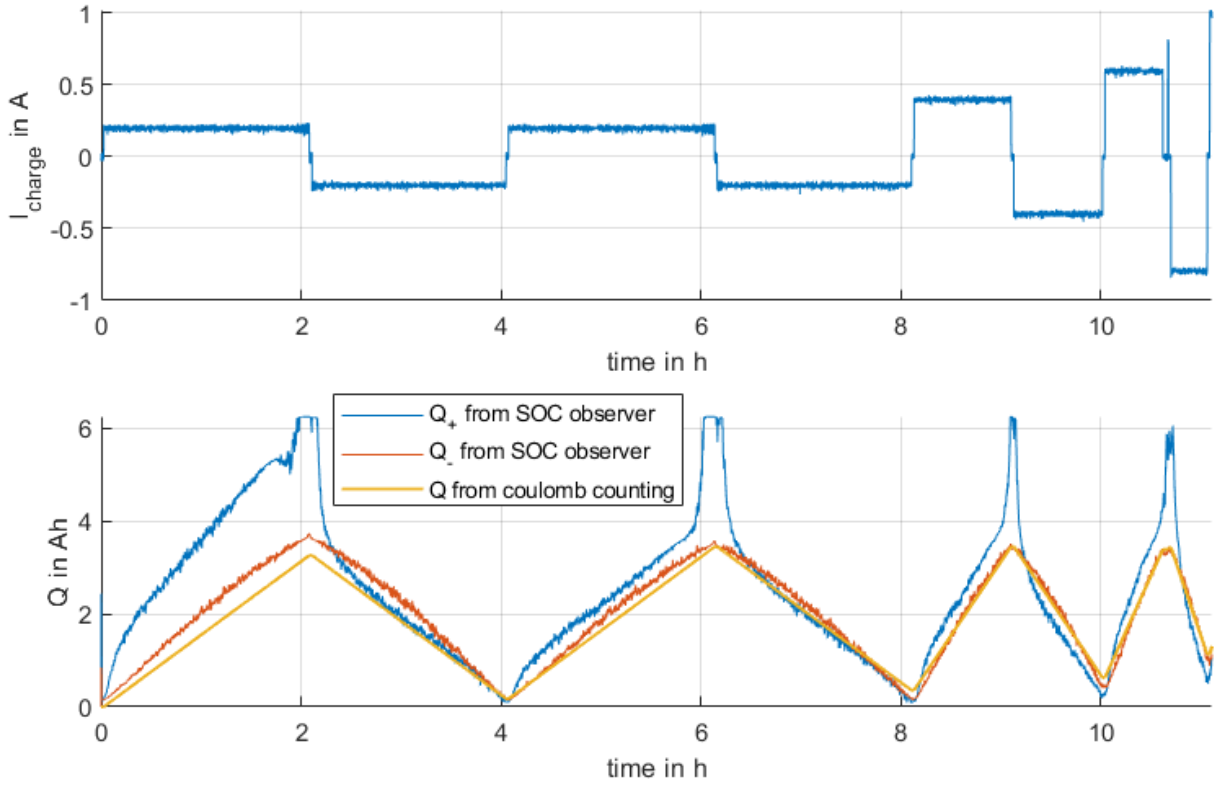

Figure 4.13.: Validation of the observer estimates.

5. Conclusion and outlook

To conclude there are basically two main objectives investigated in this thesis:

1. The development of a control of the volume flow and pressure difference across the membrane based on an underlying hydraulic model.
2. The development of an electro-chemical model to find a method for the estimation of the State-of-Charge.

Regarding the hydraulic model and control objective, it can be stated that:
The developed model is able to capture the main effects of the hydraulic system and is sufficiently accurate for control purposes. The model could also potentially be used in future to detect deposition of material in the stack or pipes through the deviation between model calculated and measured pressure. This could be one part to determine the state of health of the battery system. Additionally the model could be used to estimate the not measured volume flow of the side of the negative electrolyte.
The proposed control structure is able to react fast to a changing reference signal, while keeping the pressure difference across the membrane acceptable small. This rapid change of the volume flow allows to react accordingly to fast changing current in the battery like it would happen for operation at the grid. This will be necessary to ensure that there are enough of reactants inside the cells at all times, while not wasting unnecessary energy with pumping.

In regard to the electrochemical model and the objective of SOC estimation, it can be stated that:
The developed model is able to capture the main behaviour of the redox battery test bench. Nevertheless a more advanced model regarding the positive electrolyte, would be desirable and should be part of future investigations. This would also significantly improve the SOC-estimation of the observer presented in this work.
This thesis showed that for well estimated model parameters the presented observer works quite well. Unfortunately the measurements of the redox probes tend to drift very slowly over the time, which could lead to bad estimates. Therefore future research might go into the development of a method for an automatic recalibration of the redox probes.

Finally another goal for future research could be to combine the hydraulic and electrochemical knowledge to optimize the operation of the redox flow battery. This might be done by a model predictive reference adaptation, based on the SOC-estimates and the developed models.

Appendix

Appendix A.

Electrochemical Experiments

To characterize the electrochemical behaviour of the used electrolytes different experiments were conducted. Here the experiments are described briefly and the results are analysed. Some of the findings are relevant for the modelling.

A.1. Experiment: Battery Cycling

One of the most common experiments to study the electrochemical behaviour of batteries is the so-called cycling. Here, the battery is repeatedly charged and discharged with a constant current. Based on this experiments, different performance parameters like coulombic efficiency and cycle stability can be determined. Figure A.1 shows multiple charge/discharge cycles plotted on top of each other, where all the cycles were done for a volume flow of $\dot{V} = 1750\frac{ml}{min}$ and a current of $|I_{\text{charge}}| = 500mA$. It shows the measurement of the redox probes over the accumulated charge in the upper plot and the measured stack voltage over the accumulated charge in the bottom plot. The good overlap of all the cycles indicates a good cycle stability, which indicates that the maximum storable charge Q_{max} is constant for short time periods. The accumulated charge is bigger for charging than for discharging, leading to the gap visible in the plots of the cycle. This mismatch is commonly described by the coulombic efficiency

$$\eta_{\text{c}} = \frac{\left|\int_{t_{\text{d,0}}}^{t_{\text{d,f}}} I_{\text{charge}} dt\right|}{\left|\int_{t_{\text{c,0}}}^{t_{\text{c,f}}} I_{\text{charge}} dt\right|} \tag{A.1}$$

where $t_{\text{c,0}}$ and $t_{\text{d,0}}$ are the start times and $t_{\text{c,f}}$ and $t_{\text{d,f}}$ are finish times of the charging and discharging respectively. I_{charge} is the current defined to be positive for charging. For the conducted experiment, the coulombic efficiency was about 94%.
Another finding of figure A.1 is that there is some kind of hysteresis behaviour for the positive electrolyte. This behaviour was previously unknown, and the underlying effects are unclear at the moment. It might have to do with different reaction pathways for charging and discharging of the 2-electron process, but further chemical research is needed. Due to the missing knowledge of the underlying mechanism, this hysteresis is neglected in the modelling.

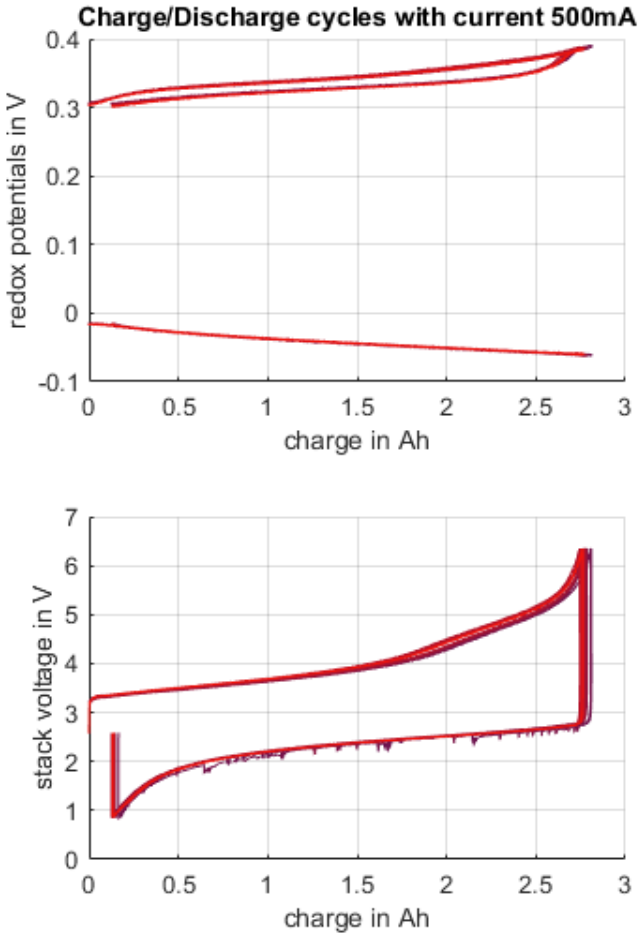

Figure A.1.: Multiple charge/discharge cycles for 500mA current plotted overlapped.
Upper plot shows the measured redox potentials over the accumulated charge. Upper line is the positive electrolyte, bottom line is the negative electrolyte.
Bottom plot shows the stack voltage over the accumulated charge.

A.2. Experiment: Changing volume flow

This experiment is very similar to the battery cycling, but for each charge/discharge cycle, another volume flow is chosen. This experiment shows the importance of the suitable volume flow for the operation of the flow battery. Figure A.2 shows the comparison of the stack voltage evolution for the different charge or discharge cycles. The lower the volume flow, the earlier the charge and discharge cycles are ended by reaching the pre-set voltage bounds of the potentiostat. This is due to the fact, that especially at the end of a cycle fewer reactants can be delivered into the cells leading to an increase of the overpotentials.

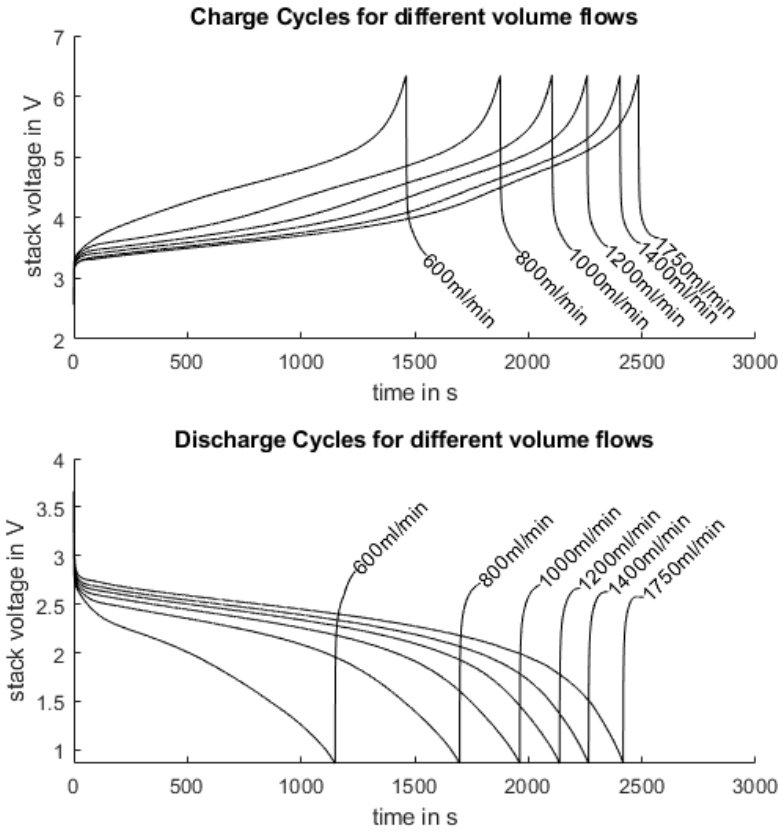

Figure A.2.: Charge and discharge curves for different volume flow through the stack, but with constant current of 500mA.

A.3. Experiment: Changing current

In this experiment, the current is changed for each cycle. Figure A.3 shows the measurement data of the experiment. The upper plot shows the cell voltage and the Open-Circuit-Voltage OCV approximated by the difference of the two redox probe measurements. The second plot shows the applied current, which is increasing step-wise from cycle to cycle. The last plot shows the measurements of the redox probes.

An increasing current leads to lower charge and discharge times. But the charge/discharge process reaches its voltage bounds already earlier in terms of the accumulated charge for higher currents. The reason is the increased consumption of reactants leading to higher overpotentials in the cell. That higher currents can only achieve a lower level of discharge or charge can be also seen in the measurements of the redox probes.

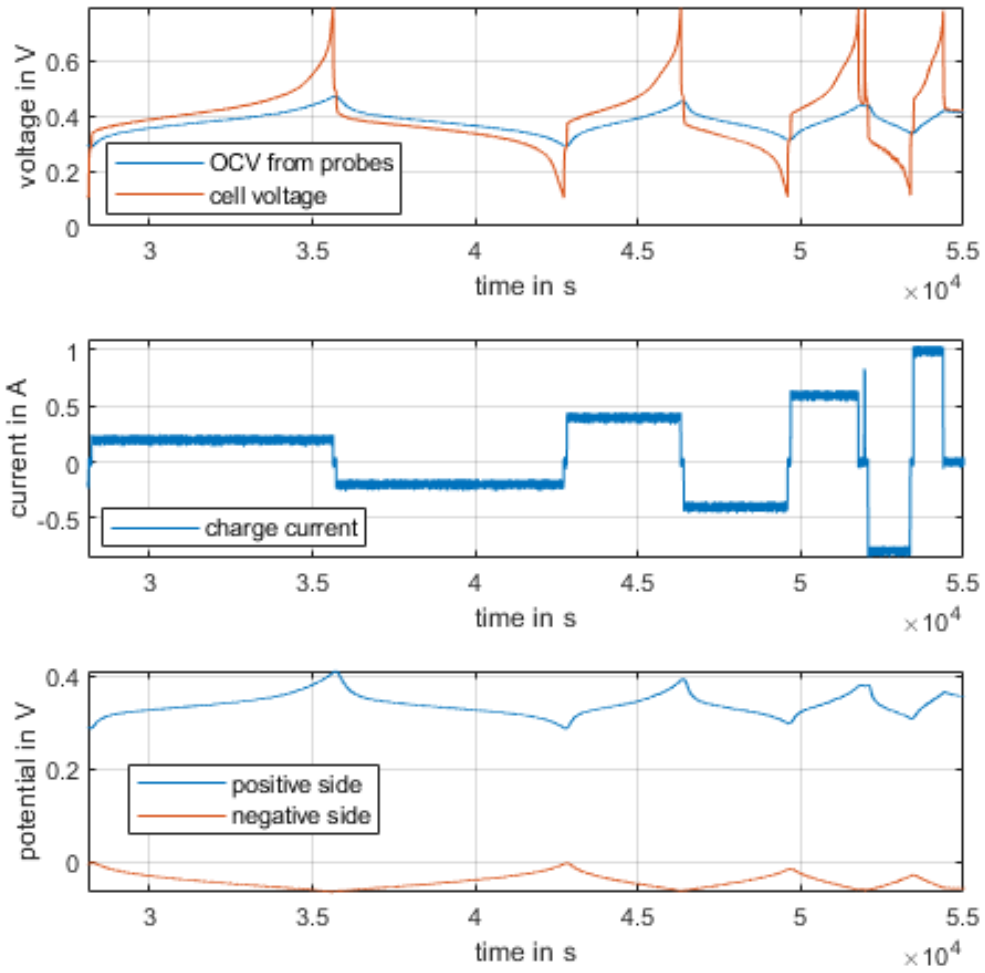

Figure A.3.: First plot: stack voltage and Open-Circuit-Voltage over time.
Second plot: step by step increased current over time.
Third plot: measurements of the redox probes for the positive and negative electrolyte.

A.4. Experiment: Stepwise charge and discharge

These experiments aim to get measurements linking the stored charge towards the corresponding Open-Circuit-Voltage OCV and the redox potentials measured at the redox probes. Therefore, the battery is brought into a defined state of nearly fully charge or discharge. This is done by charging with a constant voltage of $0.8V$ per cell and discharging with $0.1V$ per cell until the current drops beneath $50mA$. Beginning in this defined states, the battery is charged or discharged with a current pulse followed by some time for the cell voltage to relax and the concentrations in tank and cell to assimilate. These pulses are repeated. Figure A.4 shows the first two pulses of the stepwise charge experiment. The stack voltage and the OCV calculated by the potential difference of the redox probes can be seen in the upper plot. The bottom plot shows the accumulated charge.

At the end of each relaxation phase, the measurements are sampled. Figure A.5 shows

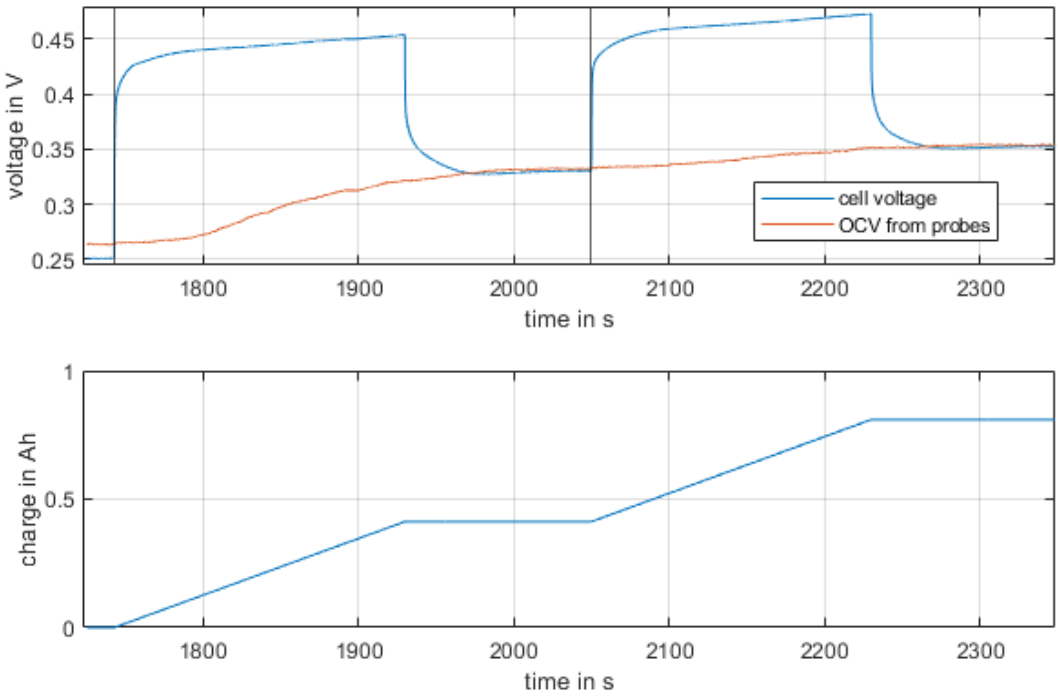

Figure A.4.: First two charge pulses of the stepwise charge experiment with the stack voltage and the OCV in the upper plot and the accumulated charge in the bottom plot.

in the upper plot the sampled potentials of the redox probes over the corresponding accumulated charge. Close inspection reveals that the positive electrolyte is limiting the amount of charge storable in the battery. This can be seen by the increasingly upward pointing trend of the positive-side electrolyte for high charge, while the same in the downward direction isn't visible for the negative-side electrolyte. The bottom plot shows OCV directly measured in the cell in comparison with the OCV calculated by the potential difference of the redox probes. One can see that the redox probes underestimate the real OCV for a high SOC, while overestimate the OCV for a low SOC. Figure A.6 shows that there is some linear dependency between them. Linear regression leads to

$$\mathrm{OCV}_{\mathrm{cell}} = k_{\mathrm{OCV}} \cdot \mathrm{OCV}_{\mathrm{probes}} + d_{\mathrm{OCV}} \tag{A.2}$$

with $k_{\mathrm{OCV}} = 1.1123$ and $d_{\mathrm{OCV}} = -0.0381V$ to describe this relation. According to the data sheets of the measurement hardware, such a linearity error can not be explained. So the reason for this linearity error is not clear, but can be considered as correction factor in the modelling.

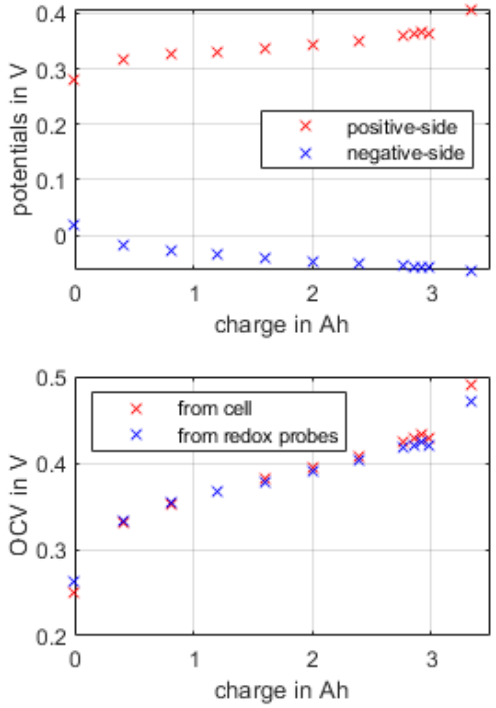

Figure A.5.: Upper plot shows the measurements of the redox probes over the accumulated charge. Bottom plot shows the OCV from the probes and directly measured over the accumulated charge.

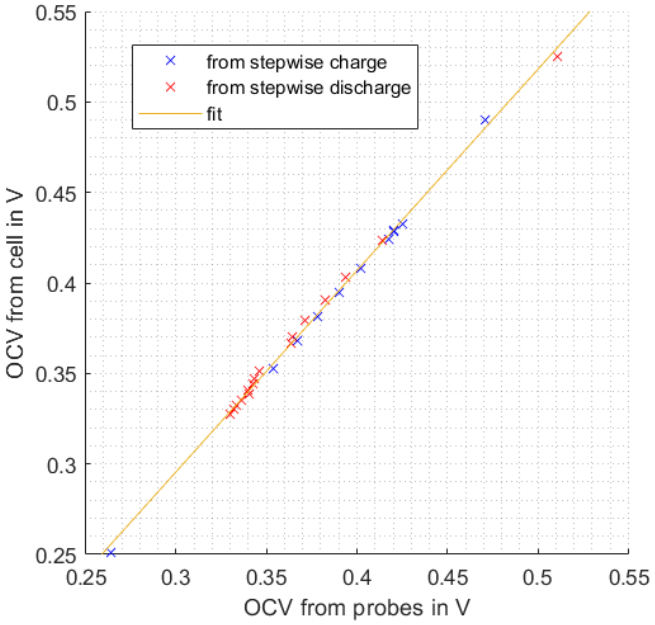

Figure A.6.: Linear relationship between the OCV of the probes and the OCV measured in the cell.

References

[1] Anya Castillo and Dennice F. Gayme. "Grid-scale energy storage applications in renewable energy integration: A survey." In: *Energy Conversion and Management* 87 (2014), pp. 885–894. ISSN: 0196-8904. DOI: https://doi.org/10.1016/j.enconman.2014.07.063. URL: https://www.sciencedirect.com/science/article/pii/S0196890414007018 (cit. on p. 1).

[2] T. Shigematsu. "Redox flow battery for energy storage." In: *SEI Technical Review* 73 (Oct. 2011), pp. 4–13 (cit. on p. 1).

[3] Piergiorgio Alotto et al. "Redox Flow Batteries for large scale energy storage." In: *2012 IEEE International Energy Conference and Exhibition (ENERGYCON)*. 2012, pp. 293–298. DOI: 10.1109/EnergyCon.2012.6347770 (cit. on p. 1).

[4] Ruiyong Chen, Sangwon Kim, and Zhenjun Chang. "Redox Flow Batteries: Fundamentals and Applications." In: *Redox*. Ed. by Mohammed Awad Ali Khalid. Rijeka: IntechOpen, 2017. Chap. 5. DOI: 10.5772/intechopen.68752. URL: https://doi.org/10.5772/intechopen.68752 (cit. on p. 1).

[5] Alejandro Clemente and Ramon Costa-Castelló. "Redox Flow Batteries: A Literature Review Oriented to Automatic Control." In: *Energies* 13 (Sept. 2020), p. 4514. DOI: 10.3390/en13174514 (cit. on p. 1).

[6] Werner Schlemmer et al. "2-Methoxyhydroquinone from Vanillin for Aqueous Redox-Flow Batteries." In: *Angewandte Chemie International Edition* 59.51 (2020), pp. 22943–22946. DOI: https://doi.org/10.1002/anie.202008253. eprint: https://onlinelibrary.wiley.com/doi/pdf/10.1002/anie.202008253. URL: https://onlinelibrary.wiley.com/doi/abs/10.1002/anie.202008253 (cit. on p. 1).

[7] Trevor J. Davies and Joseph J. Tummino. "High-Performance Vanadium Redox Flow Batteries with Graphite Felt Electrodes." In: *C* 4.1 (2018). ISSN: 2311-5629. DOI: 10.3390/c4010008. URL: https://www.mdpi.com/2311-5629/4/1/8 (cit. on p. 3).

[8] Viktor Unterberger et al. "Model-based control of hydraulic heat distribution systems — Theory and application." English. In: *Control Engineering Practice* 101 (Aug. 2020). ISSN: 1873-6939. DOI: https://doi.org/10.1016/j.conengprac.2020.104464 (cit. on pp. 8, 17).

[9] Thomas Puleston et al. "Modelling and Estimation of Vanadium Redox Flow Batteries: A Review." In: *Batteries* 8.9 (2022). ISSN: 2313-0105. DOI: 10.3390/batteries8090121. URL: https://www.mdpi.com/2313-0105/8/9/121 (cit. on p. 26).

[10] Ao Tang et al. "Investigation of the effect of shunt current on battery efficiency and stack temperature in vanadium redox flow battery." In: *Journal of Power Sources* 242 (2013), pp. 349–356. ISSN: 0378-7753. DOI: https://doi.org/10.1016/j.jpowsour.2013.05.079. URL: https://www.sciencedirect.com/science/article/pii/S0378775313008690 (cit. on p. 27).

[11] Petr Mazúr et al. "A complex four-point method for the evaluation of ohmic and faradaic losses within a redox flow battery single-cell." In: *MethodsX* 6 (2019), pp. 534–539 (cit. on p. 34).

[12] C.H. Hamann, A. Hamnett, and W. Vielstich. *Electrochemistry*. Wiley, 2007, p. 169. ISBN: 9783527310692. URL: https://books.google.at/books?id=EXljvgAACAAJ (cit. on p. 34).

[13] Yifeng Li, Maria Skyllas-Kazacos, and Jie Bao. "A dynamic plug flow reactor model for a vanadium redox flow battery cell." In: *Journal of Power Sources* 311 (2016), pp. 57–67. ISSN: 0378-7753. DOI: https://doi.org/10.1016/j.jpowsour.2016.02.018. URL: https://www.sciencedirect.com/science/article/pii/S0378775316301264 (cit. on p. 36).

[14] Ao Tang, Jie Bao, and Maria Skyllas-Kazacos. "Studies on pressure losses and flow rate optimization in vanadium redox flow battery." In: *Journal of Power Sources* 248 (2014), pp. 154–162. ISSN: 0378-7753. DOI: https://doi.org/10.1016/j.jpowsour.2013.09.071. URL: https://www.sciencedirect.com/science/article/pii/S037877531301567X (cit. on p. 36).

[15] Matthew D.R. Kok et al. "Mass transfer in fibrous media with varying anisotropy for flow battery electrodes: Direct numerical simulations with 3D X-ray computed tomography." In: *Chemical Engineering Science* 196 (2019), pp. 104–115. ISSN: 0009-2509. DOI: https://doi.org/10.1016/j.ces.2018.10.049. URL: https://www.sciencedirect.com/science/article/pii/S0009250918307711 (cit. on p. 37).

[16] Xiangkun Ma, Huamin Zhang, and Feng Xing. "A three-dimensional model for negative half cell of the vanadium redox flow battery." In: *Electrochimica Acta* 58 (2011), pp. 238–246. ISSN: 0013-4686. DOI: https://doi.org/10.1016/j.electacta.2011.09.042. URL: https://www.sciencedirect.com/science/article/pii/S001346861101423X (cit. on p. 37).

[17] Thomas Puleston et al. "Nonlinear observer for online concentration estimation in vanadium flow batteries based on half-cell voltage measurements." In: *Computers & Chemical Engineering* 185 (2024), p. 108664. ISSN: 0098-1354. DOI: https://doi.org/10.1016/j.compchemeng.2024.108664. URL: https://www.sciencedirect.com/science/article/pii/S0098135424000826 (cit. on pp. 49, 51–53, 55).